REVIEW

2D MXene-Based Materials for Electrocatalysis

Jiapeng Liu[1,2] · Wenchao Peng[1,2] · Yang Li[1,2] · Fengbao Zhang[1,2] · Xiaobin Fan[1,2]

Abstract

MXenes, as an emerging 2D material, are expected to exert a great influence on future energy storage and conversion technologies. In this review, we systematically summarize recent advances in MXene-based materials in electrocatalysis, particularly in the hydrogen evolution, oxygen evolution, oxygen reduction, nitrogen reduction, and CO_2 reduction reactions. Crucial factors influencing the properties of these materials, such as functional groups, conductivity, and interface, are discussed, and challenges to the future development of MXene-based electrocatalysts are presented.

Keywords 2D material · MXenes · Electrocatalyst · Hydrogen evolution reaction · Oxygen evolution reaction · Oxygen reduction reaction · Nitrogen reduction reaction · CO_2 reduction reaction

Introduction

Since graphene was first prepared by mechanical exfoliation in 2004 [1], various two-dimensional (2D) materials have attracted extensive attention on account of their unique physical and chemical properties [2]. These materials consist of atomically thin sheets with inherently large surface areas; they can be used extensively in various areas, such as electrocatalysis [3], photocatalysis [4], energy storage [5], membrane separation [6, 7], and biotherapy [8]. Besides graphene, a wide range of atomically thin 2D materials have also been successfully prepared, including transition metal dichalcogenides [9–11], phosphorenes [12–14], silicenes [15, 16], germanene antimonenes [17, 18], boron nitrides [19–21], and layered double hydroxides [22].

Transition metal carbides, carbonitrides, and nitrides (MXenes) are a new addition to the family of 2D materials [23]. The common form of MXene is $M_{n+1}X_nT_x$ ($n = 1, 2, 3$), where M represents an early transition metal, X represents carbon and/or nitrogen, and T_x denotes surface functional groups, such as −O, −OH, or −F [24]. MXenes have representative structures of M_2XT_x, $M_3X_2T_x$, and $M_4X_3T_x$ with n layers of X elements covered by $n + 1$ layers of M (Fig. 1) [25]. Since the first MXene, $Ti_3C_2T_x$, was synthesized in 2011, over 19 types of MXenes have been subsequently prepared, and more MXenes are predicted to exist. As-synthesized MXene-based materials are widely applied in various fields, such as in alkali metal batteries [26–29], photothermal conversion [30–32], photocatalysis [33–35], supercapacitors [36–38], and membrane separation [39–41], where they consistently show excellent performance. The outstanding electrical conductivity and hydrophilic surfaces of MXenes also ensure their stable performance as electrocatalysts in the hydrogen evolution reaction (HER) [42–44], oxygen evolution reaction (OER) [45, 46], oxygen reduction reaction (ORR) [47, 48], nitrogen reduction reaction (NRR) [49, 50], and CO_2 reduction reaction (CO_2RR) [51, 52].

Although the preparation, properties, and applications of MXenes in energy storage and conversion have been summarized [23, 25, 53–55], explorations of MXene-based materials for electrocatalysis have not been developed as quickly. Moreover, reviews focusing on MXene-based materials for electrocatalysts are scarce [56]. Therefore, new reviews covering research from the early stages of MXene-based materials to their present use in electrocatalysis, including their preparation, properties and the latest advances, are essential. In this review, we aim to describe recent progress on MXene-based materials for electrocatalysis.

✉ Xiaobin Fan
 xiaobinfan@tju.edu.cn

1 School of Chemical Engineering and Technology, Tianjin University, Tianjin 300072, China

2 State Key Laboratory of Chemical Engineering, Collaborative Innovation Center of Chemical Science and Engineering, Tianjin 300072, China
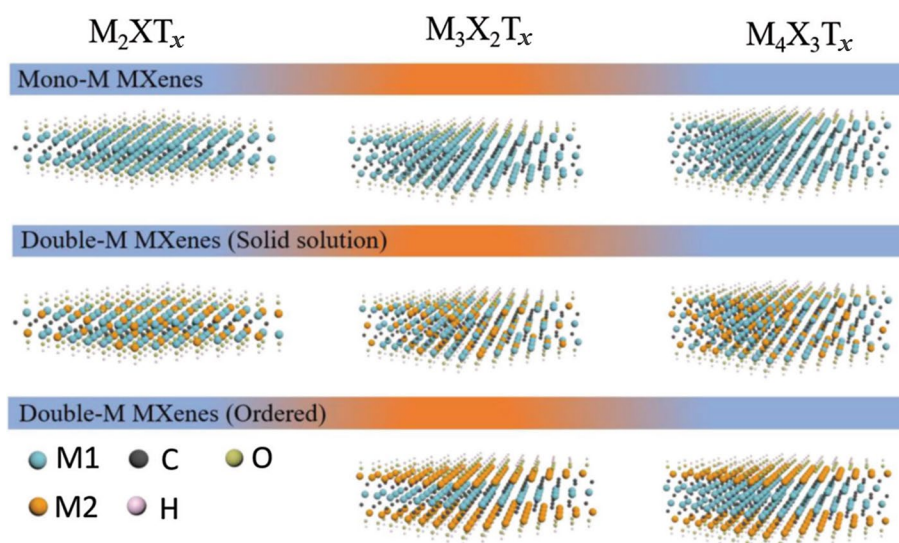
Synthesis of MXenes

MXenes are usually obtained by selective etching of specific atomic layers from their layered precursors, such as MAX phases. To date, over 70 types of MAX phases have been reported.

Since the first MXene was synthesized by etching with HF at room temperature (Fig. 2a) [57], other types of MXenes, such as TiC_2T_x [58], $Ti_3CN_xT_x$ [59], $TiNbCT_x$ [60], Mo_2CT_x [61], $Mo_2TiC_2T_x$ [62], $Mo_2Ti_2C_3T_x$ [62], V_2CT_x [61], $Ta_4C_3T_x$ [60], Nb_2CT_x [26], $Nb_4C_3T_x$ [61], $Zr_3C_2T_x$ [63], $Hf_3C_2T_x$ [64], $(Nb_{0.8}Ti_{0.2})_4C_3T_x$ [65], and $(Nb_{0.8}Zr_{0.2})_4C_3T_x$ [65], have been successfully prepared by this method. However, the aqueous HF etching method requires the handling of high-concentration HF and a strenuous multi-step procedure. Ghidiu et al. [38] proposed a safer and easier synthetic route to MXene synthesis by in situ formation of HF via the reaction of HCl and LiF. Subsequently, other fluorides, such as NaF [66], KF [66], CsF [38], CaF [38], FeF_3 [67], and tetra-*n*-butylammonium fluoride [38], have been used to synthesize MXenes. NH_4F [68] and NH_4HF_2 [69] have also been employed to synthesize MXenes (e.g., $Ti_3C_2T_x$). Some MXenes, such as Ti_4N_3, have been obtained through etching with molten fluoride salt mixtures at high temperature [70].

Although various MXenes have been achieved by etching with HF or in situ formation of HF (Fig. 2b) [71], these methods limit the large-scale preparation and application of the catalysts owing to the acute toxicity of HF. Therefore, the development of novel HF-free methods is necessary. Xuan et al. [72], for instance, presented a strategy involving the organic base-driven intercalation and delamination of TiC (Fig. 2c). In another work, Li and co-workers [73] reported that KOH in the presence of a

small amount of water can serve as an etchant to prepare MXenes (Fig. 2d). Pang et al. [74] reported a HF-free facile and rapid MXene synthesis method via thermal-assisted electrochemical etching (Fig. 2e). Li et al. [75] proposed an element-replacement approach by reaction with Lewis-acidic molten salts (Fig. 2f). Thus, future developing trends may focus on safe and efficient preparation methods for MXenes.

Structural and Electronic Properties

Structural Properties

The overall crystal geometry of MXene presents a hexagonal close-packed structure, which is analogous to its MAX-phase precursor. Here, M atoms are arranged in a close-packed structure, and octahedral sites are occupied by X atoms. The adjacent layered units are connected via van der Waals forces, similar to other 2D materials [53].

MXenes are usually prepared in aqueous solutions, including acidic fluorides. Therefore, the surface of MXenes is occupied by a mixture of −OH, −O, and −F terminations. For brevity, these molecules are denoted $M_{n+1}X_nT_x$, where T represents the surface termination. Non-terminated MXenes have never been obtained [23, 76]. Recent computational studies demonstrate that the surface termination exerts significant impacts on the properties of MXenes. For example, Hu et al. [77] systematically studied the chemical origin of termination-functionalized MXenes by Bader charge analysis and thermodynamic calculations; the materials revealed stability in the order of $Ti_3C_2O_2 > Ti_3C_2F_2 > Ti_3C_2(OH)_2 > Ti_3C_2H_2 > Ti_3C_2$, which was attributed to the splitting of the highly degenerated $3d$ orbitals of surface Ti. In another study, Fu and co-workers
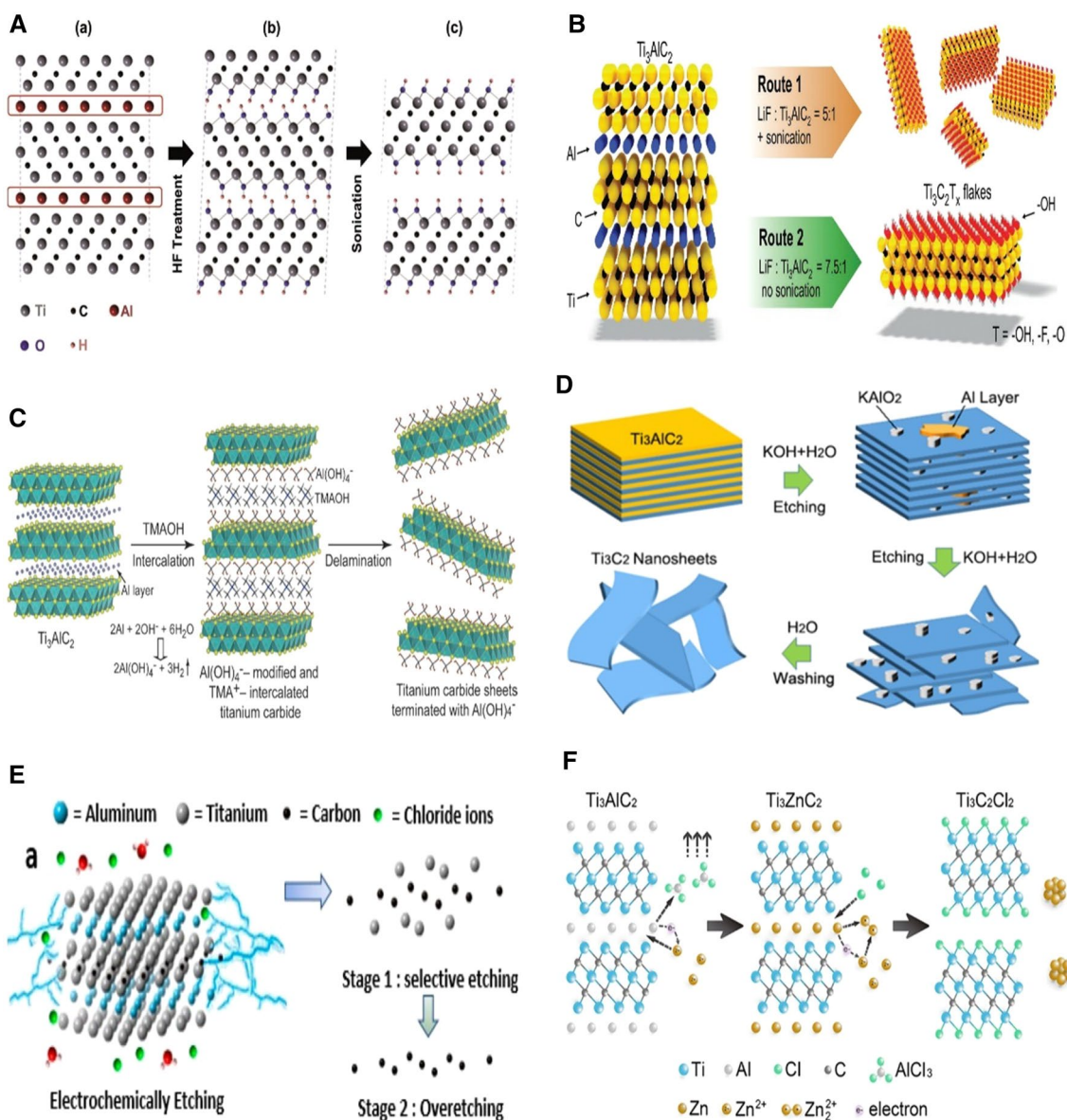
Fig. 2 Schematic of the exfoliation process of Ti$_3$AlC$_2$. **A** HF etching method. Reproduced with permission [57]. Copyright 2011, Wiley-VCH. **B** LiF+HCl etching method. Reproduced with permission [71]. Copyright 2016, Wiley-VCH. **C** Organic base (TMAOH) method. Reproduced with permission [72]. Copyright 2016, Wiley-VCH. **D** KOH method. Reproduced with permission [73]. Copy-right 2017, American Chemical Society. **E** Proposed electrochemical etching mechanism of Ti$_2$AlC in HCl electrolyte. Reproduced with permission [74]. Copyright 2019, American Chemical Society. **F** Schematic of the exfoliation process of Ti$_3$AlC$_2$ by molten ZnCl$_2$. Reproduced with permission [75]. Copyright 2019, American Chemical Society

[78] systematically explored the effects of several functional groups (i.e., −Cl, −F, −H, −O, and −OH) on the stabilization, mechanical properties, and electronic structures of a representative MXene (Ti$_3$C$_2$); the authors found that oxygen-functionalized Ti$_3$C$_2$ shows better thermodynamic stabilization and strength than their other counterparts due to significant charge transfers from inner bonds to the outer surface of the material. While MXenes with specific terminations may be gained by a post-synthesis method, very few studies on this topic have been reported. For example, Meng et al. [79] predicted that S-functionalized Ti$_3$C$_2$ displays metallic behavior, a stable structure, a low diffusion barrier, and outstanding storage capacity for Na-ion batteries.

Besides theoretical explorations, surface termination of MXenes such as Ti$_3$C$_2$T$_x$ and V$_2$CT$_x$ has also been investigated by using experimental methods. For instance, Wang et al. [80] revealed the surface atomic scale of Ti$_3$C$_2$T$_x$ through aberration-corrected scanning transmission electron microscopy (STEM); the group found that surface functional groups (e.g., −OH, −F, and −O) are randomly distributed

on the MXene surfaces and prefer to occupy the top sites of the central Ti atom. Karlsson's group [81] observed individual and double sheets of Ti_3C_2 by aberration-corrected STEM-EELS and revealed sheet coverage and intrinsic defects and TiO_x adatom complexes. In another study, Sang and co-workers [24] observed the different point defects in monolayer Ti_3C_2 nanosheets via STEM through the minimally intensive layer delamination method. Hope et al. [82] quantified the surface functional groups of $Ti_3C_2T_x$ by ^1H and ^{19}F nuclear magnetic resonance (NMR) experiments and found that the proportions of different surface terminations highly rely on the preparation method of the material. Harris et al. [83] directly measured the surface termination groups of V_2CT_x MXenes via solid-state NMR.

Electronic Properties

The applications of MXenes in electrochemistry energy storage and electrocatalysis largely rely on the inherent excellent electronic properties of the catalyst materials. Recent theoretical computational studies have been carried out to explore the effect of different M, X, and surface functional groups on the electronic properties of most MXenes. Since MXenes include various transition metals, the electronic properties of MXenes may be expected to range from metallic to semiconducting [55]. However, some MXenes have been predicted to be topological insulators because they contain heavy transition metals, such as Mo, W, and Cr [23, 25]. Additionally, surface termination could change the electronic properties of bare MXenes. For example, Fredrickson et al. [84] investigated the structural and electronic properties of layered bulk Ti_2C and Mo_2C with multiple functional groups in aqueous media by density functional theory (DFT) calculations. The out-of-plane lattice parameter of bulk MXenes is obviously affected by surface functional groups and intercalation of water. At zero applied potential, bulk MXenes (Ti_2C and Mo_2C) were functionalized by one monolayer of O. However, bare MXenes were unstable, regardless of the applied potential. In addition, changes in the surface functional groups of Ti_2C from O-covered to H-covered could promote metal–insulator transition under an applied potential. In another study, Tang et al. [28] reported that bare MXenes (e.g., Ti_3C_2) show metallic properties; however, functionalizing Ti_3C_2 with different groups (e.g., –OH, –F, and –I) yields semiconductor properties with narrow band gaps. This study also demonstrated that the M layer could obviously affect the electronic properties of the resulting material. Interestingly, whereas $Ti_3C_2T_x$ is metallic, MXenes containing Mo display semiconductor properties. Wang and Liao [85] reported that Ni_2N MXenes show intrinsic half-metallicity using DFT calculations. The electronic properties of MXene have been related to their nanostructures. Enyashin and Ivanovskii [86], for instance, predicted that

hydroxylated Ti_3C_2 nanotubes have metallic-like characteristics. Zhao et al. [87] predicted that Ti_3C_2 nanoribbons have distinct electronic properties different from those of MXenes nanosheets.

Several experiments have been performed to study the electronic properties of MXenes. However, only the electronic properties of some MXenes, such as Ti_2CT_x, $Ti_3C_2T_x$, and Mo_2CT_x, have been experimentally evaluated thus far [55]. For example, Halim et al. [88] evaluated the electronic conduction of $Ti_3C_2T_x$ and Mo_2CT_x films. Lipatov and co-workers [71] measured the electronic properties of monolayer $Ti_3C_2T_x$ flakes. Lai et al. [89] revealed the excellent electronic properties of 2D Ti_2CT_x. Computational and experimental results demonstrate that MXenes have excellent electronic properties and are promising candidate materials for electrochemistry, energy storage, and electrocatalysis.

Applications in Electrocatalysis

In the following section, we summarize current progress on the applications of MXene-based materials in electrocatalysis, including HER, OER, ORR, NRR, and CO_2RR, as presented in Table 1.

Hydrogen Evolution Reaction

Hydrogen is a promising energy carrier that may be harnessed to solve energy and environmental problems due to its high energy density and environmental friendliness. Electrochemical water splitting via HER offers the possibility of obtaining hydrogen through a clean and sustainable strategy. Pt-based catalysts display excellent performance for HER, but their high cost and scarcity seriously hinder their practical applications [121, 122]. Therefore, exploring earth-abundant electrocatalysts that can potentially replace Pt is of paramount importance. As described earlier, MXenes exhibit outstanding electronic properties due to their inherent metallic character. Thus, the development of MXene-based HER electrocatalysts has attracted extensive attention.

Several theoretical calculations and experiments on MXene-based catalysts have been carried out to explore their applications in HER. Seh et al. [90] first performed a combined theoretical calculation and experimental study on pristine MXenes as electrocatalysts for HER. DFT calculations revealed that Mo_2CT_x is a promising candidate HER catalyst, as shown in Fig. 3a, b. Experiments indicated that Mo_2CT_x requires an overpotential of 189 mV to reach a current density of 10 mA/cm^2 (Fig. 3c) and, thus, is superior to Ti_2CT_x. In addition, theoretical calculations indicate that the basal planes of Mo_2CT_x could act as active sites for HER,

Table 1 Summary of the current progress on MXene-based materials as electrocatalysts

Catalyst	Application	Performance	Electrolyte	References
Mo_2CT_x	HER	189 mV at 10 mA/cm^2	0.5 mol/L H_2SO_4	[90]
$Ti_3C_2T_x$	HER	538 mV at 10 mA/cm^2	0.5 mol/L H_2SO_4	[91]
F-terminated Ti_2CT_x	HER	170 mV at 10 mA/cm^2	0.5 mol/L H_2SO_4	[92]
O-terminated $Ti_3C_2T_x$	HER	190 mV at 10 mA/cm^2	0.5 mol/L H_2SO_4	[44]
$V_4C_3T_x$	HER	200 mV at 10 mA/cm^2	0.5 mol/L H_2SO_4	[93]
N-Ti_2CT_x	HER	215 mV at 10 mA/cm^2	0.5 mol/L H_2SO_4	[94]
$Ti_3C_2T_x$ nanofibers	HER	169 mV at 10 mA/cm^2	0.5 mol/L H_2SO_4	[95]
$Ni_{0.9}Co_{0.1}$@Nb-$Ti_3C_2T_x$	HER	43.4 mV at 10 mA/cm^2	1.0 mol/L KOH	[43]
Pt/$Ti_3C_2T_x$-550	HER	32.7 mV at 10 mA/cm^2	0.1 mol/L $HClO_4$	[96]
TBA-$Ti_3C_2T_x$-Pt-20	HER	70 mV at 10 mA/cm^2	0.5 mol/L H_2SO_4	[97]
Co^{3+}-Cr_2CT_x	HER	404 mV at 10 mA/cm^2	1.0 mol/L KOH	[74]
Co^{3+}-V_2CT_x	HER	460 mV at 10 mA/cm^2	1.0 mol/L KOH	[74]
Co^{3+}-Ti_2CT_x	HER	458 mV at 10 mA/cm^2	1.0 mol/L KOH	[74]
Co-MoS_2@Mo_2CT_x	HER	112 mV at 10 mA/cm^2	1.0 mol/L KOH	[98]
PtNPs/$Ti_3C_2T_x$	HER	226 mV at 10 mA/cm^2	0.1 mol/L H_2SO_4	[99]
$MoS_2\perp Ti_3C_2$	HER	110 mV at 10 mA/cm^2	0.5 mol/L H_2SO_4	[100]
PtO_aPdO_bNPs@$Ti_3C_2T_x$	HER	57 mV at 10 mA/cm^2	0.5 mol/L H_2SO_4	[101]
$Ni_{0.9}Fe_{0.1}PS_3$@ $Ti_3C_2T_x$	HER	196 mV at 10 mA/cm^2	1.0 mol/L KOH	[102]
MoS_2/Ti_3C_2-MXene@C	HER	135 mV at 10 mA/cm^2	0.5 mol/L H_2SO_4	[103]
MoS_2/$Ti_3C_2T_x$ nanoroll	HER	168 mV at 10 mA/cm^2	0.5 mol/L H_2SO_4	[42]
$Mo_2TiC_2T_x$-Pt_{SA}	HER	30 mV at 10 mA/cm^2	0.5 mol/L H_2SO_4	[104]
CoP@3D $Ti_3C_2T_x$	HER	168 mV at 10 mA/cm^2	1.0 mol/L KOH	[105]
FeNi-LDH/$Ti_3C_2T_x$	OER	298 mV at 10 mA/cm^2	1.0 mol/L KOH	[45]
CoNi-ZIF-67@$Ti_3C_2T_x$	OER	323 mV at 10 mA/cm^2	1.0 mol/L KOH	[106]
$Ti_3C_2T_x$-CoBDC	OER	410 mV at 10 mA/cm^2	0.1 mol/L KOH	[107]
g-C_3N_4/$Ti_3C_2T_x$ film	OER	420 mV at 10 mA/cm^2	0.1 mol/L KOH	[108]
Co-B_i/$Ti_3C_2T_x$	OER	250 mV at 10 mA/cm^2	1.0 mol/L KOH	[46]
S-$NiFe_2O_4$@Ti_3C_2@NF	OER	270 mV at 10 mA/cm^2	1.0 mol/L KOH	[109]
NiCoS/$Ti_3C_2T_x$	OER	365 mV at 10 mA/cm^2	1.0 mol/L KOH	[110]
Co^{3+}-Cr_2CT_x	OER	420 mV at 10 mA/cm^2	1.0 mol/L KOH	[74]
Co^{3+}-V_2CT_x	OER	420 mV at 10 mA/cm^2	1.0 mol/L KOH	[74]
Co^{3+}-Ti_2CT_x	OER	420 mV at 10 mA/cm^2	1.0 mol/L KOH	[74]
PtO_aPdO_bNPs@$Ti_3C_2T_x$	OER	310 mV at 10 mA/cm^2	0.1 mol/L KOH	[101]
$Ni_{0.7}Fe_{0.3}PS_3$@ $Ti_3C_2T_x$	OER	282 mV at 10 mA/cm^2	1.0 mol/L KOH	[102]
Co/N-CNTs@$Ti_3C_2T_x$	OER	411 mV at 10 mA/cm^2	0.1 mol/L KOH	[111]
CoP@3D $Ti_3C_2T_x$	OER	280 mV at 10 mA/cm^2	1.0 mol/L KOH	[105]
g-C_3N_4/$Ti_3C_2T_x$	ORR	0.79 V at half-wave potential	0.1 mol/L KOH	[47]
FeNC/$Ti_3C_2T_x$	ORR	0.81 V at half-wave potential	0.1 mol/L KOH	[112]
$Ti_3C_2T_x$/NW-$Ag_{0.9}Ti_{0.1}$	ORR	0.78 V at half-wave potential	0.1 mol/L KOH	[113]
FePc/$Ti_3C_2T_x$	ORR	0.86 V at half-wave potential	0.1 mol/L KOH	[48]
Mn_3O_4/$Ti_3C_2T_x$	ORR	0.89 V at onset potential	0.1 mol/L KOH	[114]
FeCo(3:1)-N-d-Ti_3C_2	ORR	0.80 V at half-wave potential	0.1 mol/L KOH	[115]
Ultrathin $Ti_3C_2T_x$	ORR	0.85 V at onset potential	0.1 mol/L KOH	[116]
Co/N-CNTs@$Ti_3C_2T_x$	ORR	0.81 V at half-wave potential	0.1 mol/L KOH	[111]
TiO_2/$Ti_3C_2T_x$	NRR	26.32 µg/(h mg$_{cat}$) 8.42% faradaic efficiency at -0.60 V	0.1 mol/L HCl	[117]
F-free $Ti_3C_2T_x$	NRR	26.32 µg/(h mg$_{cat}$) 9.1% faradaic efficiency at -0.3 V	0.1 mol/L HCl	[118]
$Ti_3C_2T_x$/FeOOH	NRR	4.72 µg/(h cm^2) at -0.1 V 5.78% faradaic efficiency at -0.2 V	0.5 mol/L Li_2SO_4 (pH = 2 adjusted by 1 mol/L HCl)	[49]
$Ti_3C_2T_x$	NRR	20.4 µg/(h mg$_{cat}$) 9.3% faradaic efficiency at -0.4 V	0.1 mol/L HCl	[119]

Catalyst	Application	Performance	Electrolyte	References
MnO_2-$Ti_3C_2T_x$	NRR	34.12 μg/(h mg$_{cat}$) 11.39% faradaic efficiency at -0.55 V	0.1 mol/L HCl	[120]
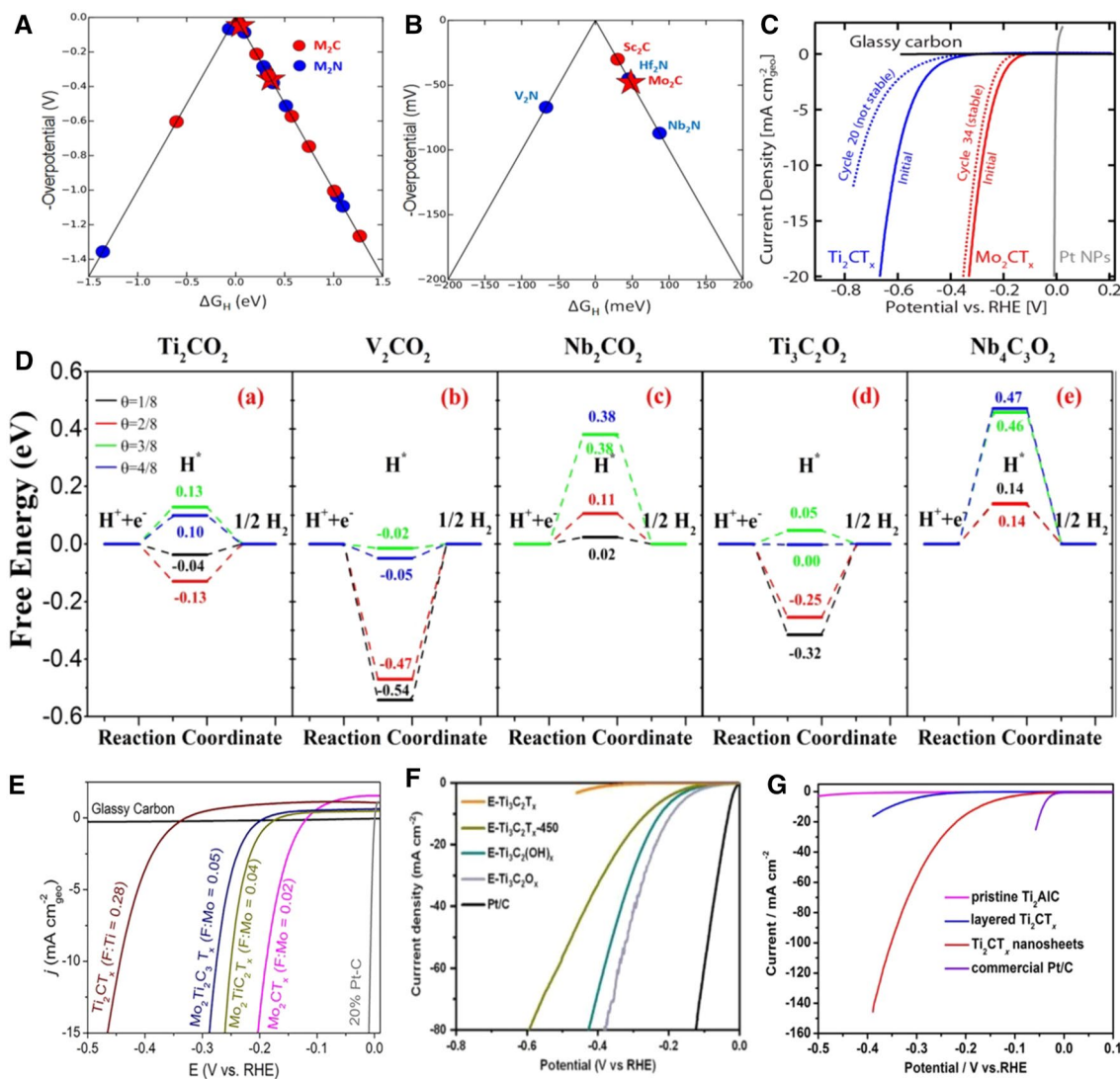
Fig. 3 **A** HER volcano curves with theoretical overpotentials for the studied MXenes. The stars represent two MXenes (Ti$_2$C and Mo$_2$C) in the experiment. **B** Zoomed-in portion of the top of the volcano in **A**. **C** Polarization curves of Ti$_2$CT$_x$ and Mo$_2$CT$_x$ nanosheets and Pt nanoparticles. Reproduced with permission [90]. Copyright 2016, American Chemical Society. **D** Free energy diagrams of HER processing on Ti$_2$CO$_2$, V$_2$CO$_2$, Nb$_2$CO$_2$, Ti$_3$C$_2$O$_2$, and Nb$_4$C$_3$O$_2$. Reproduced with permission [123]. Copyright 2016, American Chemical Society. **E** Polarization curves of glassy carbon, Ti$_3$C$_2$T$_x$ (F:Ti$=0.28$), Mo$_2$Ti$_2$C$_3$T$_x$ (F:Mo$=0.05$), Mo$_2$TiC$_2$T$_x$ (F:Mo$=0.04$), Mo$_2$CT$_x$ (F:Mo$=0.02$), and 20% Pt/C. Reproduced with permission [91]. Copyright 2018, American Chemical Society. **F** Polarization curves of E-Ti$_3$C$_2$T$_x$, E-Ti$_3$C$_2$(OH)$_x$, E-Ti$_3$C$_2$O$_x$, E-Ti$_3$C$_2$T$_x$-450, and Pt/C. Reproduced with permission [44]. Copyright 2011, Wiley-VCH. **G** Polarization curves of pristine Ti$_2$AlC, layered Ti$_2$CT$_x$ nanosheets, and Pt/C. Reproduced with permission [124]. Copyright 2018, Elsevier Ltd

which is clearly different from the mechanism of the widely studied 2H phase MoS$_2$.

Gao et al. [123] studied the HER performance of various O-terminated 2D MXenes, such as Ti$_2$C, V$_2$C, Nb$_2$C, Ti$_3$C$_2$, and Nb$_4$C$_3$, by DFT calculations. As shown in Fig. 3d, different MXenes displayed different Gibbs free energies for the adsorption of atomic hydrogen (ΔG_{H*0}) under different coverages. Among the MXenes tested, Ti$_3$C$_2$O$_2$ notably

showed the lowest ΔG_{H*0} with a hydrogen coverage of 4/8. The ΔG_{H*0} of Cr_2CO_2 MXene with different hydrogen coverages has also been obtained by Cheng et al. [92].

Theoretical calculations indicate that modifying the surface functional groups of MXenes is an effective route to boost their HER performance, and many of these results have been verified by experiments. For example, Handoko et al. [91] first investigated the effect of five MXenes with different F coverages on their basal plane for HER and found that the presence of F terminations deteriorates the HER performance of these materials. As-obtained Mo_2CT_x featuring low F coverage only required 189 mV to achieve a current density of 10 mA/cm^2 (Fig. 3e). Besides, oxygen groups on the basal planes of Mo_2CT_x proved to be catalytically active for HER. Jiang et al. [44] prepared oxygen-functionalized ultrathin $Ti_3C_2T_x$ and achieved a HER performance (190 mV at 10 mA/cm^2) higher than that of untreated $Ti_3C_2T_x$, as shown in Fig. 3f. Li et al. [124] synthesized rich F-terminated Ti_2CT_x and obtained excellent HER performance with a small overpotential of 170 mV at a current density of 10 mA/cm^2 (Fig. 3g). $V_4C_3T_x$ MXene has also been synthesized and directly used as a HER catalyst [93].

Yoon et al. [94] synthesized nitrided-Ti_2CT_x (N-Ti_2CT_x) via the high-temperature nitridation of 2D Ti_2CT_x using NaNH$_2$ (Fig. 4a). As shown in Fig. 4b, the obtained N-Ti_2CT_x showed high HER catalytic performance with an overpotential of 215 mV at a current density of 10 mA/cm^2, which is over three times smaller than that of pristine-Ti_2CT_x (645 mV). The effects of nanostructures on the

HER catalytic activity of MXenes have been explored. For instance, Yang et al. [125] constructed 12 types of MXenes nanoribbon models and evaluated the role of MXenes nanoribbon edges on catalyzing HER. Nanoribbons of Ti_3C_2 and solid solution (Ti, Nb)C showed outstanding performance for HER and revealed low adsorption free energies (close to 0 eV) and small Tafel barriers below 0.42 and 0.17 eV, respectively (Fig. 4c–e). $Ti_3C_2T_x$ MXene nanofibers were successfully prepared by Yuan and co-workers [95], and the obtained nanofibers displayed enhanced HER activity with a small overpotential of 169 mV at 10 mA/cm^2 (Fig. 4f) and a Tafel slope of 97 mV/dec.

Hybridizing active components with MXene is yet another effective route to improve HER catalytic activity. Thus, the development of MXene-based nanohybrids has drawn wide attention. You et al. [126] predicted that Schottky barrier-free hole contacts could be formed at six MXenes (i.e., $V_4C_3O_2$, Mo_2CO_2, V_2NO_2, Cr_2NO_2 Cr_2CO_2, and V_2CO_2) and 2H-MoS$_2$ contacting interfaces. The formation of unique interfaces was attributed to the high work functions of the MXenes (Fig. 5a), which were larger than the ionization energy of monolayer 2H-MoS$_2$, and the absence of the formation of interfacial gap states that usually strongly pin the Fermi level in the midgap of the semiconductor. The authors also found that efficient charge injection into MoS$_2$ facilitated by the Schottky barrier-free contact could also increase the HER activity of the 2H-MoS$_2$ basal plane by improving its conductivity as well as its ability to adsorb hydrogen, being comparable to 1T-MoS$_2$ (Fig. 5b, c).
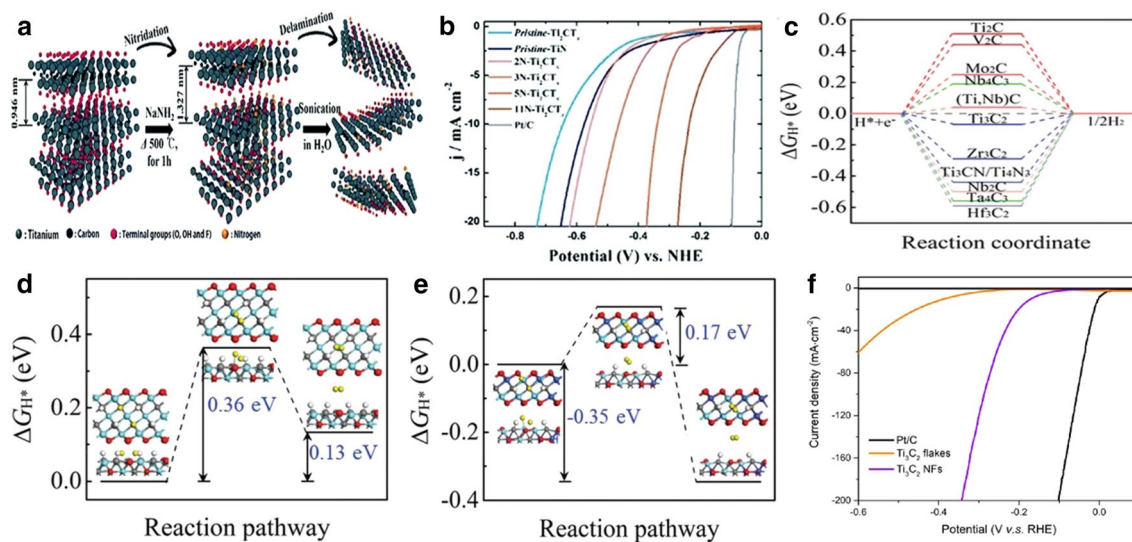
Fig. 4 a Preparations of the N-Ti_2CT_x nanosheets. b Polarization curves of Ti_2CT_x with different nitridation degrees, pristine-Ti_2CT_x, TiN, and Pt/C. Reproduced with permission [94]. Copyright 2018, Royal Society of Chemistry. c Free energy diagrams for hydrogen evolution on the edges of various MXene nanoribbons. Free energy profiles of the Tafel reaction for H$_2$ formation on d the edges of Ti_3C_2 and e (Ti, Nb)C MXene nanoribbons, respectively. Reproduced with permission [125]. Copyright 2018, Royal Society of Chemistry. f Polarization curves of Ti_3C_2 flakes, Ti_3C_2 nanofibers, and Pt/C. Reproduced with permission [95]. Copyright 2018, American Chemical Society
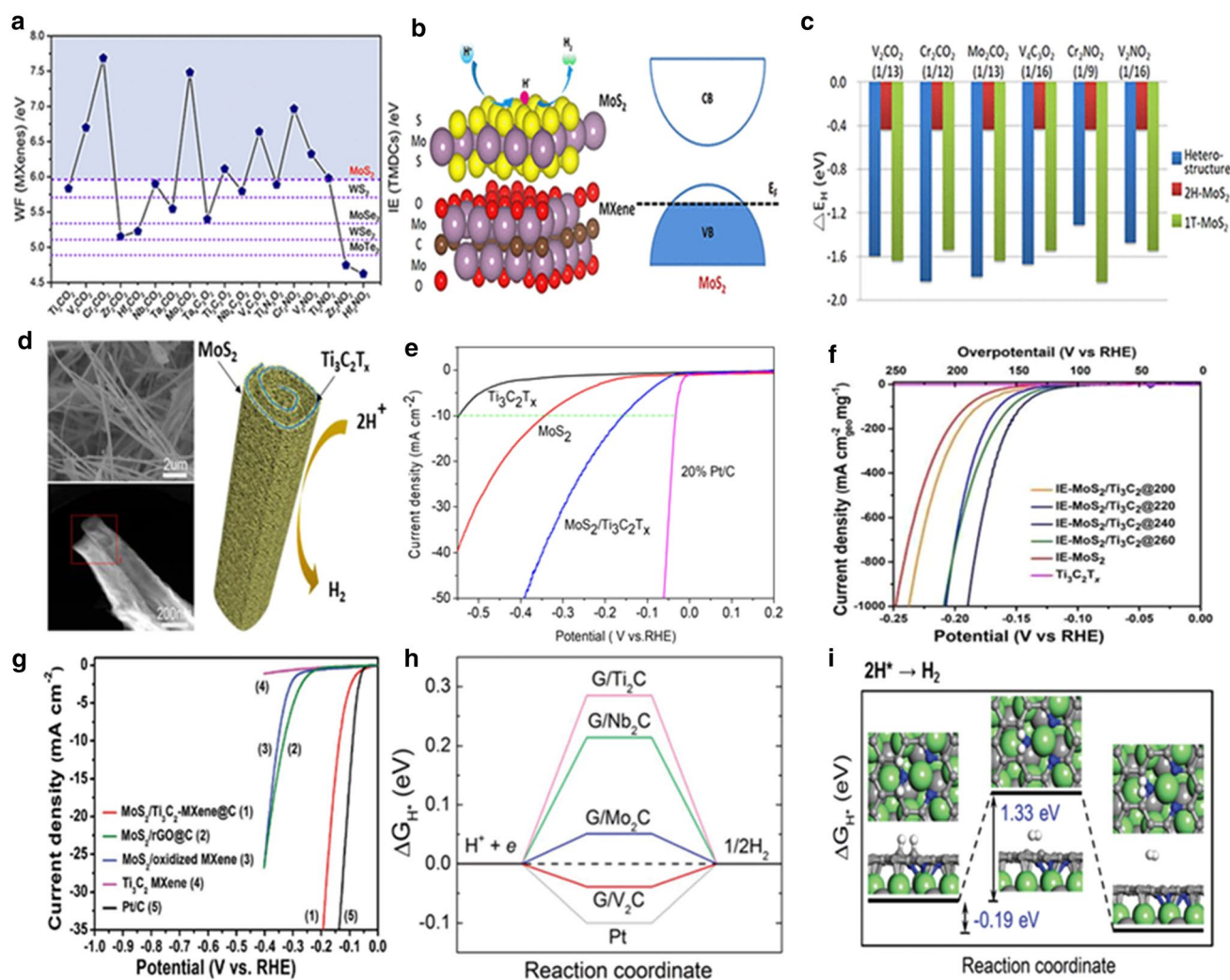
Fig. 5 **a** Work functions (denoted by dots) of different MXenes with O terminations compared with the ionization energies (denoted by dashed lines) of monolayer MoS_2, WS_2, $MoSe_2$, WSe_2, and $MoTe_2$. **b** Schematic of the MoS_2-catalyzed HER and metallic energy-band feature of MoS_2 induced by *p*-type Schottky barrier-free contact. **c** Hydrogen adsorption energies of 2H-MoS_2, 1T-MoS_2, and 2H-MoS_2/MXene heterostructures. The numbers in brackets represent the corresponding different H coverages. Reproduced with permission [126]. Copyright 2019, American Chemical Society. **d** Typical TEM and SEM images of a nanoroll-like MoS_2/$Ti_3C_2T_x$ hybrid and schematic of the MoS_2/$Ti_3C_2T_x$-catalyzed HER process. **e** Polarization curves of a MoS_2/$Ti_3C_2T_x$ hybrid, pure MoS_2, $Ti_3C_2T_x$ nanosheets, and Pt/C. Reproduced with permission [42]. Copyright 2019, Elsevier Ltd. **f** Polarization curves of interlayer expanded-MoS_2/Ti_3C_2 at various temperatures. Reproduced with permission [100]. Copyright 2018, Royal Society of Chemistry. **g** Polarization curves of MoS_2/Ti_3C_2-MXene@C, MoS_2/oxidized MXene, MoS_2/rGO@C, Ti_3C_2 MXene, and Pt/C catalysts. Reproduced with permission [103]. Copyright 2011, Wiley-VCH. **h** Reaction free energy (ΔG_{H*}) of HER on the most active sites of different graphene/MXene heterostructures and on the Pt (111) surface. **i** Changes in ΔG_{H*} during HER on N-doped graphene over a V_2C MXene monolayer. Reproduced with permission [128]. Copyright 2018, Royal Society of Chemistry

In another study, Ling et al. [127] used DFT calculations to predict that a low S vacancy concentration (~ 2.5%) in MoS_2/MXenes-OH heterostructures could result in the ideal free energy needed to enhance hydrogen evolution. The simulation results indicated that the HER catalytic performance of MoS_2 could be remarkably improved by forming heterostructure with MXenes. These findings were also verified by recent experimental studies. For instance, our group developed a facile method to prepare hierarchical nanoroll-like

MoS_2/$Ti_3C_2T_x$ hybrids by combining liquid nitrogen-freezing and annealing (Fig. 5d) [42]. The resulting unique hierarchical MoS_2/$Ti_3C_2T_x$ nanohybrid showed outstanding HER catalytic activity with a low onset overpotential of 30 mV (Fig. 5e) and an over-25-fold increase in exchange current density compared with MoS_2. Attanayake et al. [100] prepared vertically aligned interlayer expanded MoS_2 on a 2D Ti_3C_2 MXene by the microwave-assisted method. The resultant few-layered MoS_2 showed a uniform interlayer spacing

of 9.4 Å and delivered a small onset potential of 95 mV (Fig. 5f) and Tafel slope (~ 40 mV/dec). Wu et al. [103] presented hierarchical MoS_2/Ti_3C_2-MXene@C nanohybrids by coupling MoS_2 nanosheets on carbon-stabilized Ti_3C_2 MXene. The obtained catalyst exhibited excellent performance with a low overpotential of 135 mV at 10 mA/cm² and a low Tafel slope of 45 mV/dec; these values are smaller than those of other counterpart catalysts (Fig. 5g). Indeed, our group presented $Co-MoS_2/Mo_2CT_x$ nanohybrids by engineering Co-doped MoS_2 coupled with Mo_2CT_x MXene [98]. The resulting hybrids exhibited a low overpotential of 112 mV at 10 mA/cm² and good stability in 1 mol/L KOH aqueous solution.

Du et al. [102] reported the in situ growth of the Ni-based bimetal phosphorus trisulfide ($Ni_{1-x}Fe_xPS_3$) on the surface of $Ti_3C_2T_x$ MXene nanosheets by a simple self-assembly and subsequent solid-state reaction process. The optimized hybrids ($Ni_{0.7}Fe_{0.3}PS_3$@MXene) exhibited a low overpotential of 196 mV for HER in 1 mol/L KOH solution. Zhou et al. [128] theoretically designed several heterostructures of N-doped graphene/MXenes (Ti_2C, Nb_2C, V_2C, and Mo_2C) as catalysts for HER. DFT calculations suggested that N-doped graphene/heterostructures possess the lowest reaction free energies (close to 0 eV) and a low Tafel reaction barrier (1.3 eV) for HER (Fig. 5g, h) owing to the strong electronic coupling between the MXene and N-doped graphene.

Recent studies indicate that the HER performance of MXenes could be improved by doping with metal atoms. Li et al. [129] studied the HER properties of modified M_2XO_2-type MXenes bearing transition metal atoms by high-throughput computational methods. Addition of transition metal atoms to several combinations, such as $Os-Ta_2CO_2$, $Ir-Sc_2CO_2$, $Ag-Nb_2NO_2$, $Re-Nb_2NO_2$, and $W-Nb_2NO_2$, could change the relevant reaction mechanism (from Volmer–Heyrovsky to Volmer–Tafel), induce electron redistributions on the surface of the MXene, and, ultimately, result in distinct enhancements in HER activity. Du et al. [43] reported an MXene ($Ti_3C_2T_x$)-based hybrid with simultaneous Nb doping and surface Ni/Co alloy modification. DFT calculations indicated that Nb doping could shift the Fermi energy level toward the conduction band, leading to improved conductivity. Moreover, the surface M–H affinity was modified by the Ni/Co alloy, and the optimized catalyst showed the lowest Gibbs free energy for adsorbed H* (Fig. 6a, b). The resultant $Ni_{0.9}Co_{0.1}$@NTM (Nb-doped $Ti_3C_2T_x$) hybrids delivered excellent HER performance, only requiring a small overpotential of 43.4 mV to deliver a current density of 10 mA/cm² in 1 mol/L KOH solution (Fig. 6c, d), and exhibited long-term stability. Using in situ co-reduction, Li et al. [96] prepared $Pt/Ti_3C_2T_x$ via alloying Pt with Ti from the surface of $Ti_3C_2T_x$. In situ X-ray absorption spectroscopy revealed that Pt transforms from a single atom into intermetallic compounds with increasing temperature (Fig. 6e). The as-prepared $Pt/Ti_3C_2T_x$-550 showed outstanding HER performance and only needed a low overpotential of 32.7 mV at 10 mA/cm² (Fig. 6f); it also demonstrated a small Tafel slope of 32.3 mV/dec. HER current normalization processing revealed that the respective mass activity and specific activity of $Pt/Ti_3C_2T_x$-550 are 4.4 and 13 times higher than those of Pt/Vulcan at an overpotential of 70 mV (Fig. 6g, h). As shown in Fig. 6i, DFT calculations demonstrated that (100)- and (111)-terminated Pt_3Ti nanoparticles show H* binding comparable with Pt (111). However, (110)-termination showed that H* adsorption was excessively exergonic, leading to poisoning of the relative overpotential.

In another work, Zhang et al. [104] reported a novel electrochemical exfoliation method to prepare $Mo_2TiC_2T_x$ MXene nanosheets for HER. The obtained nanosheets possessed an abundance of exposed basal planes and Mo vacancies providing numerous active sites on which to immobilize single atoms and improve the HER catalytic property of the MXenes (Fig. 7a). Pt atoms anchored onto the $Mo_2TiC_2T_x$ nanosheets showed excellent catalytic performance. The obtained $Mo_2TiC_2T_x$–Pt_{SA} catalysts only needed low overpotentials of 30 and 77 mV to deliver current densities of 10 and 100 mA/cm², respectively. The as-prepared catalyst showed an outstanding mass activity of 8.3 A/mg, which is around 40 times greater than that of commercial Pt/C (0.21 A/mg; Fig. 7b, c). Strong covalent bonding between $Mo_2TiC_2T_x$ and positively charged Pt atoms endowed the $Mo_2TiC_2T_x$–Pt_{SA} catalyst with outstanding long-term stability. DFT calculations suggested that single-atom Pt could lead to the redistribution of the electronic structure of $Mo_2TiC_2T_x$ and move up the d orbitals-electron domination close to the Fermi level (Fig. 7d, e), resulting in improved catalytic activity. As presented in Fig. 7f, the obtained $Mo_2TiC_2T_x$–Pt_{SA} catalyst showed a low adsorption energy of − 0.08 eV, which is significantly lower than those of $Mo_2TiC_2O_2$ (− 0.19 eV) and Pt/C (− 0.10 eV). Other Pt-modified MXenes nanohybrids have been achieved by different methods, such as photo-induced reduction [97], $NaBH_4$ reduction [99], and solution plasma modification [101], and the resulting hybrids generally showed remarkably improved performance for HER compared with pristine MXenes. Xiu et al. [105] synthesized CoP-3D MXene hybrids and studied their catalytic performance for HER. The obtained nanohybrids showed a low overpotential of 168 mV at a current density of 10 mA/cm² in 1 mol/L KOH solution. This superior electrocatalytic activity could be attributed to the hierarchical 3D architecture of the catalysts, which greatly boosts their active surface area, promotes higher charge transfer kinetics, and increases their mass diffusion rate.
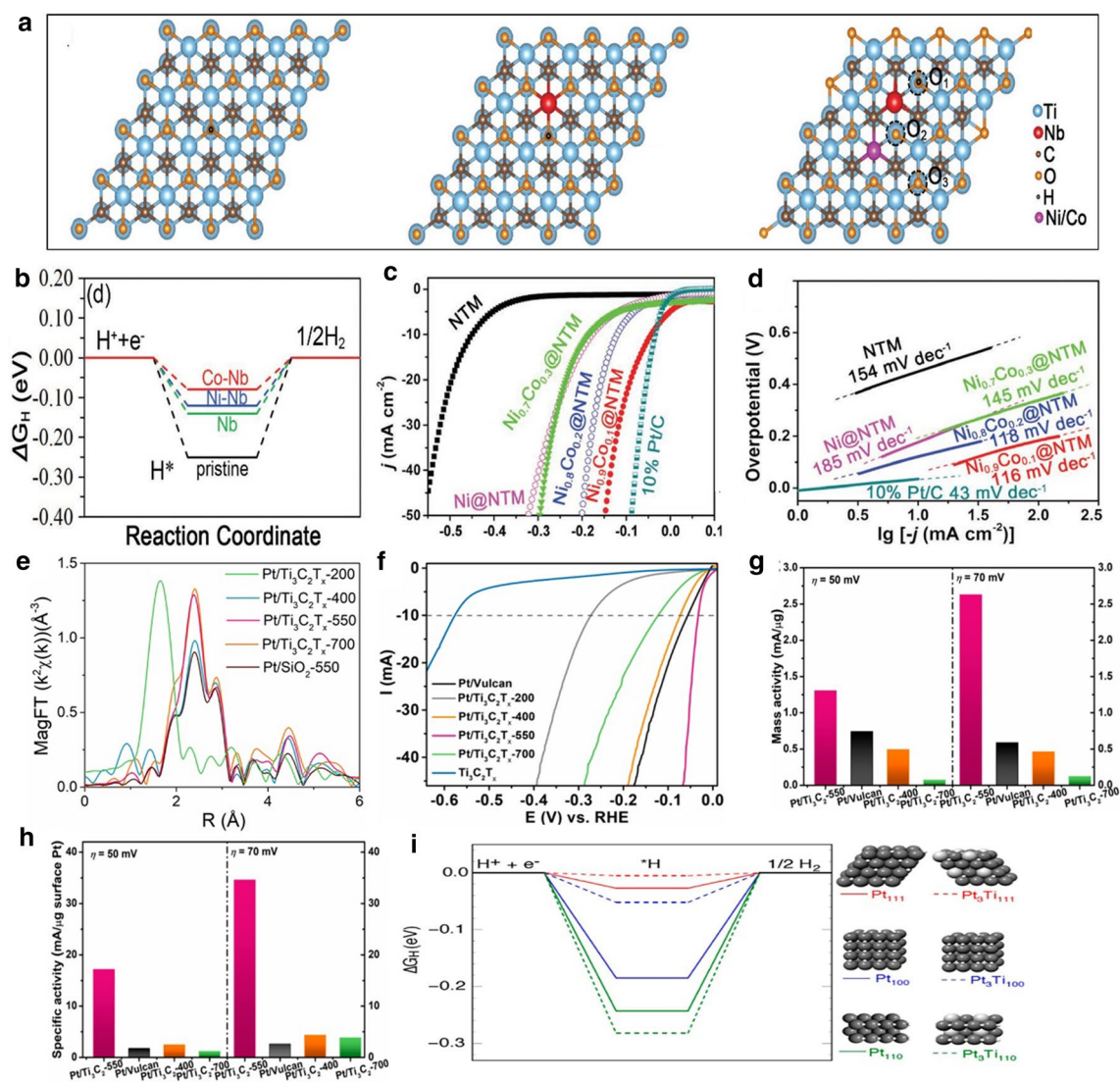
Fig. 6 a Atomistic configuration of pristine monolayer $Ti_3C_2O_2$ with H* adsorption, Nb doped on pristine monolayer $Ti_3C_2O_2$ with H* adsorption, Co/Ni replacement of Ti atoms on Nb-doped pristine monolayer $Ti_3C_2O_2$, and the three different H* adsorption O sites. **b** Gibbs free energies for H* adsorbed on active sites shown in **a** M-doped $Ti_3C_2O_2$. **c** Polarization curves of a series of NiCo@Nb-doped $Ti_3C_2T_x$ MXene nanohybrids, Ni@Nb-doped $Ti_3C_2T_x$ MXene nanohybrid, Nb-doped $Ti_3C_2T_x$ MXene, and Pt/C in 1 mol/L KOH. **d** Corresponding Tafel plots of a series of NiCo@Nb-doped $Ti_3C_2T_x$ MXene nanohybrids, Ni@Nb-doped $Ti_3C_2T_x$ MXene nanohybrid, Nb-doped $Ti_3C_2T_x$ MXene, and Pt/C in 1 mol/L KOH. Reproduced with permission [43]. Copyright 2019, Wiley-VCH. **e** Magnitude of the Fourier transform of the k^2 weighted Pt L_{III} edge in situ EXAFS of Pt/$Ti_3C_2T_x$ reduced at different temperatures compared with that of Pt/SiO_2. **f** Polarization curves of Pt/Vulcan, Pt/$Ti_3C_2T_x$ at different temperatures, and $Ti_3C_2T_x$. **g** Mass activity of Pt/Vulcan and Pt/$Ti_3C_2T_x$ catalysts with different treatments. **h** Specific activity of Pt/Vulcan and Pt/$Ti_3C_2T_x$ catalysts. **i** DFT-calculated free energy diagrams of hydrogen evolution at the Pt (111), Pt_3Ti (111), Pt (100), Pt_3Ti (100), Pt (110), and Pt_3Ti (110) surfaces. Reproduced with permission [96]. Copyright 2019, American Chemical Society

Oxygen Evolution Reactions

OER plays a crucial role in many important renewable energy conversion and storage methods, such as electrochemical water splitting and metal–air batteries. Nevertheless, the sluggish kinetics and high overpotential of OER make it imperative to search for high-performance catalysts. Noble-metal-based oxides (e.g., RuO_2 and IrO_2) are high-performance catalysts for OER, but their high cost and scarcity seriously hamper their broader applications [130]. Hence, great efforts have been devoted to develop earth-abundant and high-activity catalysts that can replace precious metal-based materials.

MXene-based materials have received extensive attention for their potential applications in OER. For instance, Yu et al. [45] prepared hierarchical FeNi-LDH/$Ti_3C_2T_x$
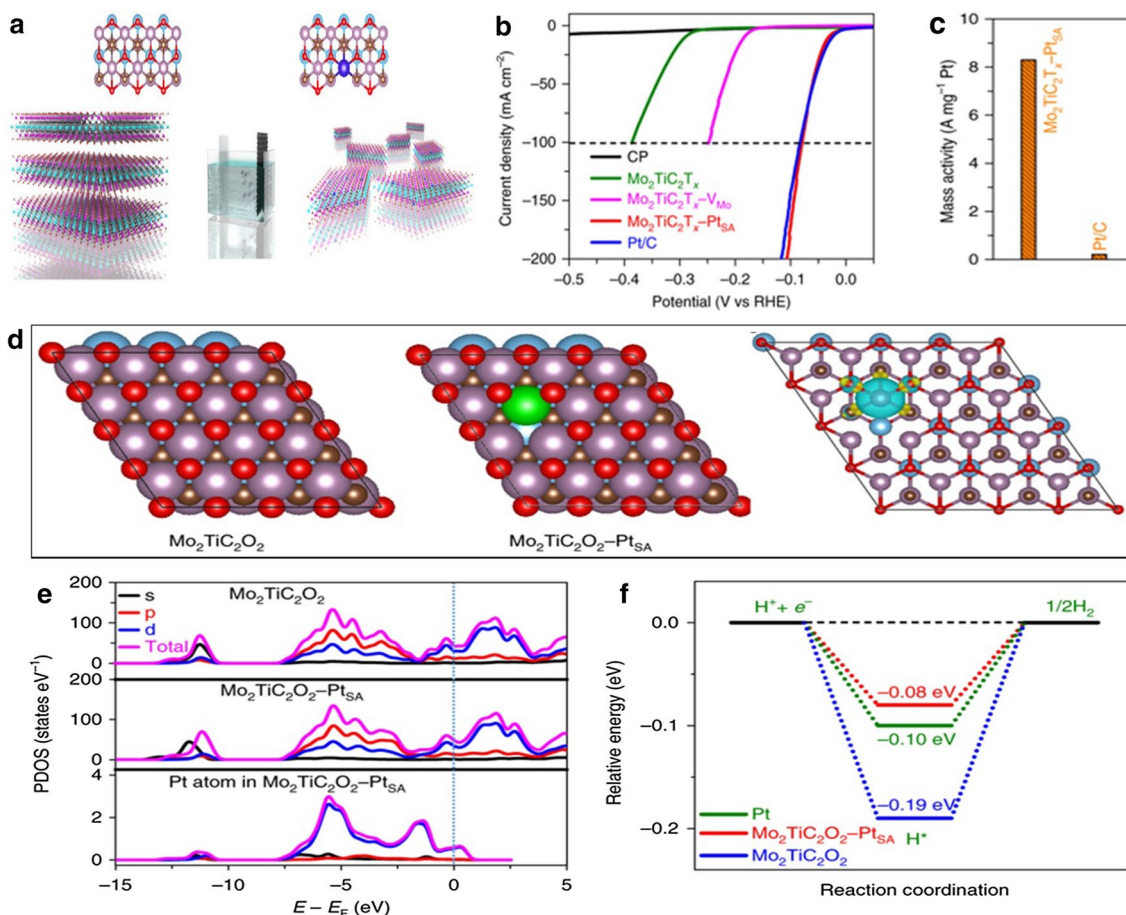
Fig. 7 a Schematic of the electrochemical exfoliation process of MXene with immobilized single Pt atoms. **b** Polarization curves of carbon paper, $Mo_2TiC_2T_x$, $Mo_2TiC_2T_x–V_{Mo}$, $Mo_2TiC_2T_x–Pt_{SA}$, and Pt/C. **c** Mass activity of state-of-the-art Pt/C and $Mo_2TiC_2T_x–Pt_{SA}$. **d** Top view of the slab models used to describe $Mo_2TiC_2O_2$ and $Mo_2TiC_2O_2–Pt_{SA}$. Circles in blue, purple, green, brown, and red represent Ti, Mo, Pt, C, and O atoms, respectively. Charge density distribution differences between $Mo_2TiC_2O_2$ and $Mo_2TiC_2O_2–Pt_{SA}$ are also shown. **e** Calculated PDOS of $Mo_2TiC_2O_2$ and $Mo_2TiC_2O_2–Pt_{SA}$ with aligned Fermi levels. **f** Free energy profiles of HER on $Mo_2TiC_2O_2$, $Mo_2TiC_2O_2–Pt_{SA}$ and Pt/C. Reproduced with permission [104]. Copyright 2018, Nature Publishing Group

nanohybrids by coprecipitation of Ni^{2+} and Fe^{3+} in the presence of $Ti_3C_2T_x$ and urea (Fig. 8a). The as-synthesized hybrids showed superior OER activity and only needed a low overpotential of 298 mV to deliver a current density of 10 mA/cm^2; they also demonstrated a low Tafel slope of 43 mV/dec (Fig. 8b–e). This achievement could be attributed to strong interfacial interactions and electronic coupling with prominent charge transfers between $Ti_3C_2T_x$ and FeNi-LDH. Such interaction and coupling not only enhance the conductivity and stability but also obviously facilitate the redox process of FeNi-LDH for OER. Ma et al. [108] prepared free-standing flexible films via the layer-by-layer self-assembly of graphitic carbon nitride (g-C_3N_4) and titanium carbide (Ti_3C_2), as shown in Fig. 8f. The obtained hierarchically porous films featured a highly hydrophilic surface and showed good OER activity; indeed, the catalysts only needed a small overpotential of 420 mV to achieve a current density of 10 mA/cm^2 and revealed a small Tafel

slope of 74.6 mV/dec in 0.1 mol/L KOH solution (Fig. 8i, j). Such excellent performance was attributed to the Ti–N_x motifs of the catalyst, which act as electroactive sites. This hypothesis was verified by XPS and near-edge X-ray absorption fine structure spectroscopy (Fig. 8g, h). Tang and coworkers [109] constructed S-NiFe$_2$O$_4$@Ti$_3$C$_2$@NF hybrids and studied their OER performance. The obtained hybrids displayed a low overpotential of 270 mA at a current density of 20 mA/cm^2 and a small Tafel slope of 46.8 mV/dec in 1 mol/L KOH solution.

Interestingly, metal organic framework (MOF) and MOF derivatives have also been successfully hybridized with MXene nanosheets to achieve improved OER performance. For example, Zhao et al. [107] synthesized an MXene/MOF hybrid ($Ti_3C_2T_x$–CoBDC) via an interdiffusion reaction-assisted method (Fig. 9a). The resultant hybrids needed a low overpotential of 410 mV to deliver a current density of 10 mA/cm^2 and showed a low Tafel slope of 48.2 mV/
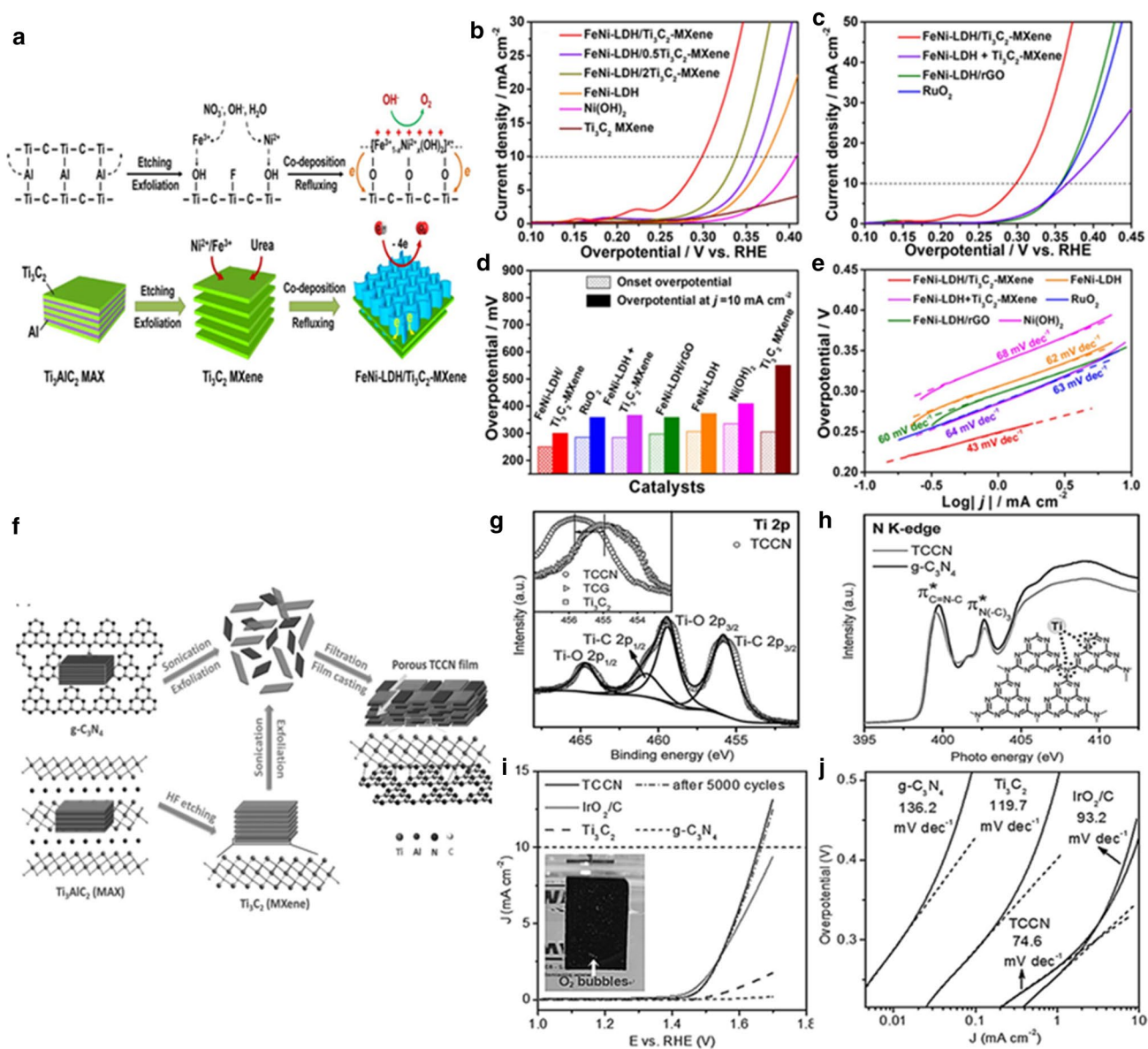
Fig. 8 **a** Schematic of the preparation of 2D hierarchical FeNi-LDH/Ti$_3$C$_2$-MXene nanohybrids. **b** Polarization curves of FeNi-LDH/Ti$_3$C$_2$-MXene with different FeNi-LDH contents, pure FeNi-LDH, Ni(OH)$_2$, and pristine Ti$_3$C$_2$ MXene. **c** Polarization curves of FeNi-LDH/Ti$_3$C$_2$-MXene with 80 wt% FeNi-LDH, FeNi-LDH + Ti$_3$C$_2$-MXene, FeNi-LDH/rGO, and RuO$_2$ catalysts. **d** Comparison of the catalysts in **b** in terms of onset overpotential and overpotential required to achieve a current density of 10 mA/cm^2. **e** Tafel plots of FeNi-LDH/Ti$_3$C$_2$-MXene, FeNi-LDH + Ti$_3$C$_2$-MXene, FeNi-LDH/ rGO, FeNi-LDH, Ni(OH)$_2$, and RuO$_2$ catalysts. Reproduced with permission [45]. Copyright 2018, Elsevier Ltd. **f** Preparation of porous Ti$_3$C$_2$/g-C$_3$N$_4$ hybrid films. **g** High-resolution XPS spectra of Ti 2p in the Ti$_3$C$_2$/g-C$_3$N$_4$ hybrid film in (**f**). **h** N K-edge NEXAFS of TCCN and g-C$_3$N$_4$; the inset displays the relevant N sites. **i** Polarization curves of the Ti$_3$C$_2$/g-C$_3$N$_4$ hybrid film, g-C$_3$N$_4$, Ti$_3$C$_2$, and IrO$_2$/C. **j** Tafel plots of the Ti$_3$C$_2$/g-C$_3$N$_4$ hybrid film, g-C$_3$N$_4$, Ti$_3$C$_2$, and IrO$_2$/C. Reproduced with permission [108]. Copyright 2016, Wiley-VCH

dec in 0.1 mol/L KOH solution (Fig. 9b, c). This superior OER performance could be attributed to the well-defined interface between the CoBDC layer and Ti$_3$C$_2$T$_x$ nanosheets, which allows fast charge and ion transfer. The presence of metallic Ti$_3$C$_2$T$_x$ nanosheets not only prevents the porous CoBDC layers from aggregating but also improves charge and ion transfers. In another study, CoNi-ZIF-67@Ti$_3$C$_2$T$_x$

was prepared via a simple coprecipitation reaction [106]. Owing to the presence of Ti$_3$C$_2$T$_x$, the CoNi-ZIF-67 particles became smaller in size, and the average oxidation of Co/Ni elements increased, thus endowing the catalyst with excellent OER performance. The CoNi-ZIF-67@Ti$_3$C$_2$T$_x$ hybrids showed a low onset potential of 275 mA versus RHE and a Tafel slope of 65.1 mV/dec. Zou et al. [110] prepared
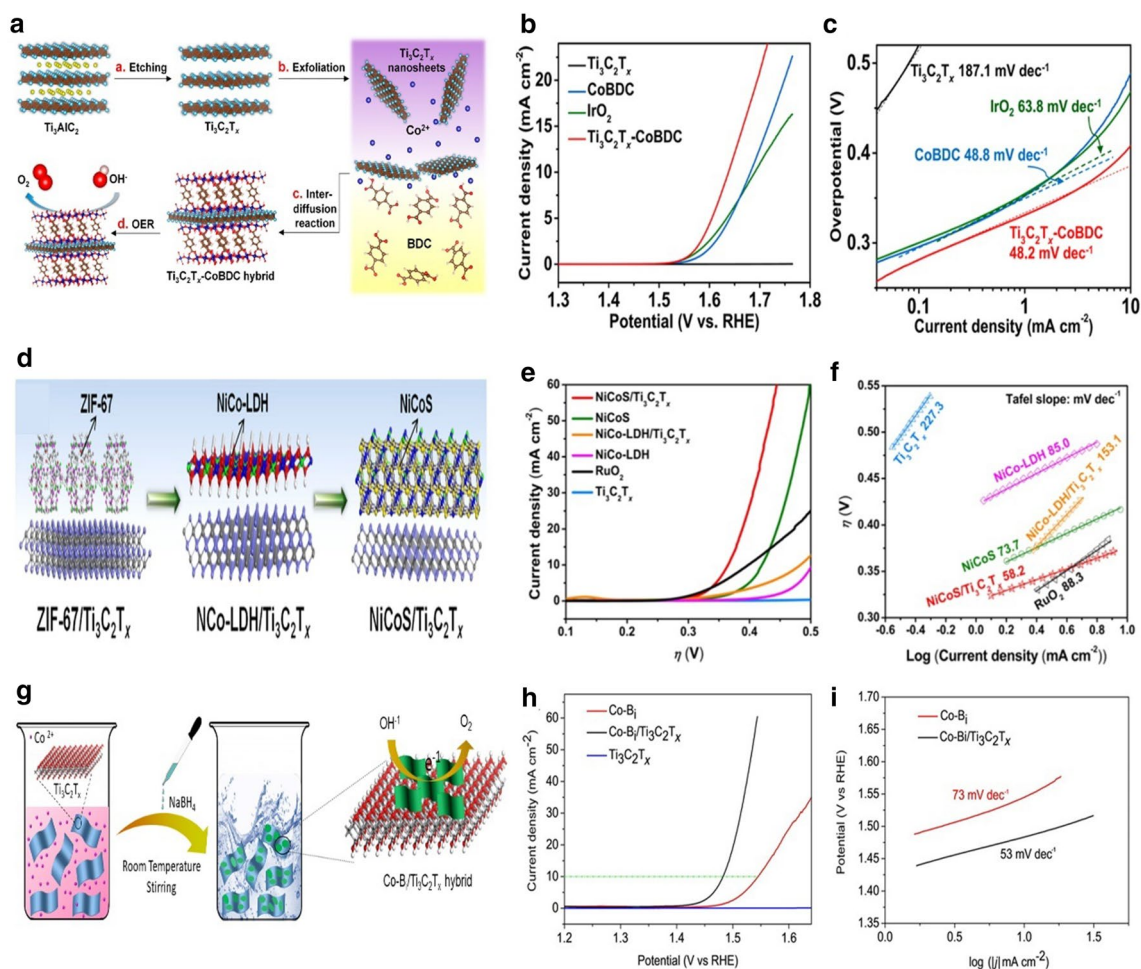
Fig. 9 **a** Preparation procedures of $Ti_3C_2T_x$–CoBDC hybrids for OER. **b** Polarization curves and **c** the corresponding Tafel plots of various electrodes modified by $Ti_3C_2T_x$, CoBDC, IrO_2, and a $Ti_3C_2T_x$–CoBDC hybrid in 0.1 mol/L KOH solution. Reproduced with permission [107]. Copyright 2017, American Chemical Society. **d** Synthesis of NiCoS/$Ti_3C_2T_x$ hybrids. **e** Polarization curves and **f** the corresponding Tafel plots of NiCoS/$Ti_3C_2T_x$, NiCoS, NiCo-LDH/ $Ti_3C_2T_x$, NiCo-LDH, and RuO_2. Reproduced with permission [110]. Copyright 2018, American Chemical Society. **g** Preparation of hierarchical Co-B_i/$Ti_3C_2T_x$ hybrids at room temperature. **h** Polarization curves and **i** the corresponding Tafel plots of Co-B_i nanosheets, a Co-B_i/$Ti_3C_2T_x$ hybrid, and $Ti_3C_2T_x$ nanosheets. Reproduced with permission [46]. Copyright 2018, Wiley-VCH

a novel NiCoS/$Ti_3C_2T_x$ hybrid using an MOF-based method (Fig. 9d). The hybrids showed a small overpotential of 365 mV at 10 mA/cm², a small Tafel slope of 58.2 mV/dec (Fig. 9e, f), and excellent stability.

Many new MXene-based hybrids also show promising applications in OER. For example, we synthesized a unique hierarchical cobalt borate/$Ti_3C_2T_x$ MXene (Co-B_i/$Ti_3C_2T_x$) by a rapid chemical reaction at room temperature (Fig. 9g) [46]. The metallic $Ti_3C_2T_x$ nanosheets not only improved the electron transfer capacity of the material but also hindered the aggregation of Co-B_i nanosheets. The strong interaction between $Ti_3C_2T_x$ and Co-B_i nanosheets ensured strong charge transfer abilities and enhanced the electrostatic attraction of more anionic intermediates to achieve fast redox processes. Thus, the as-synthesized hybrids exhibited

outstanding OER performance with a low overpotential of 250 mV at 10 mA/cm² and a small Tafel slope of 53 mV/ dec (Fig. 9h, i).

Oxygen Reduction Reaction

ORR is the key half-reaction in renewable energy conversion devices; it is characterized by inherent environmental friendliness and low cost and has been applied to fuel cells and rechargeable metal–air batteries. However, ORR often suffers from sluggish kinetics, which seriously hinders the overall power performance of these devices. Today, Pd-based catalysts are regarded as the optimal ORR catalyst [131]. However, developing low-cost and high-efficiency catalysts for ORR remains a crucial endeavor.

Liu and Li [132] simulated a series of Pt/*v*-Ti$_{n+1}$C$_n$T$_x$ (*n* = 1–3, T = O and/or F) heterostructures by DFT calculations. As displayed in Fig. 10a, F-terminated MXenes were predicted to display better performance in ORR than their O-terminated counterparts; however, F-terminated MXenes may demonstrate lower stability on account of their weaker chemical bonding. A variety of MXene-based materials have been explored to enhance ORR performance. For instance, Li et al. [48] prepared FePc/Ti$_3$C$_2$T$_x$ hybrids

by a facile self-assembly method in dimethylformamide solution. Owing to the presence of Ti$_3$C$_2$T$_x$, obvious Fe 3*d* electron delocalization and spin-state transition of Fe(II) ions were confirmed by a series of characterization analysis, such as ESR and Mössbauer spectroscopy, as presented in Fig. 10b–d. More importantly, changes in electron configuration led to lower local electron densities and higher spin states in the Fe(II) centers, which promoted oxygen adsorption and reduction in active FeN$_4$ sites. As shown in
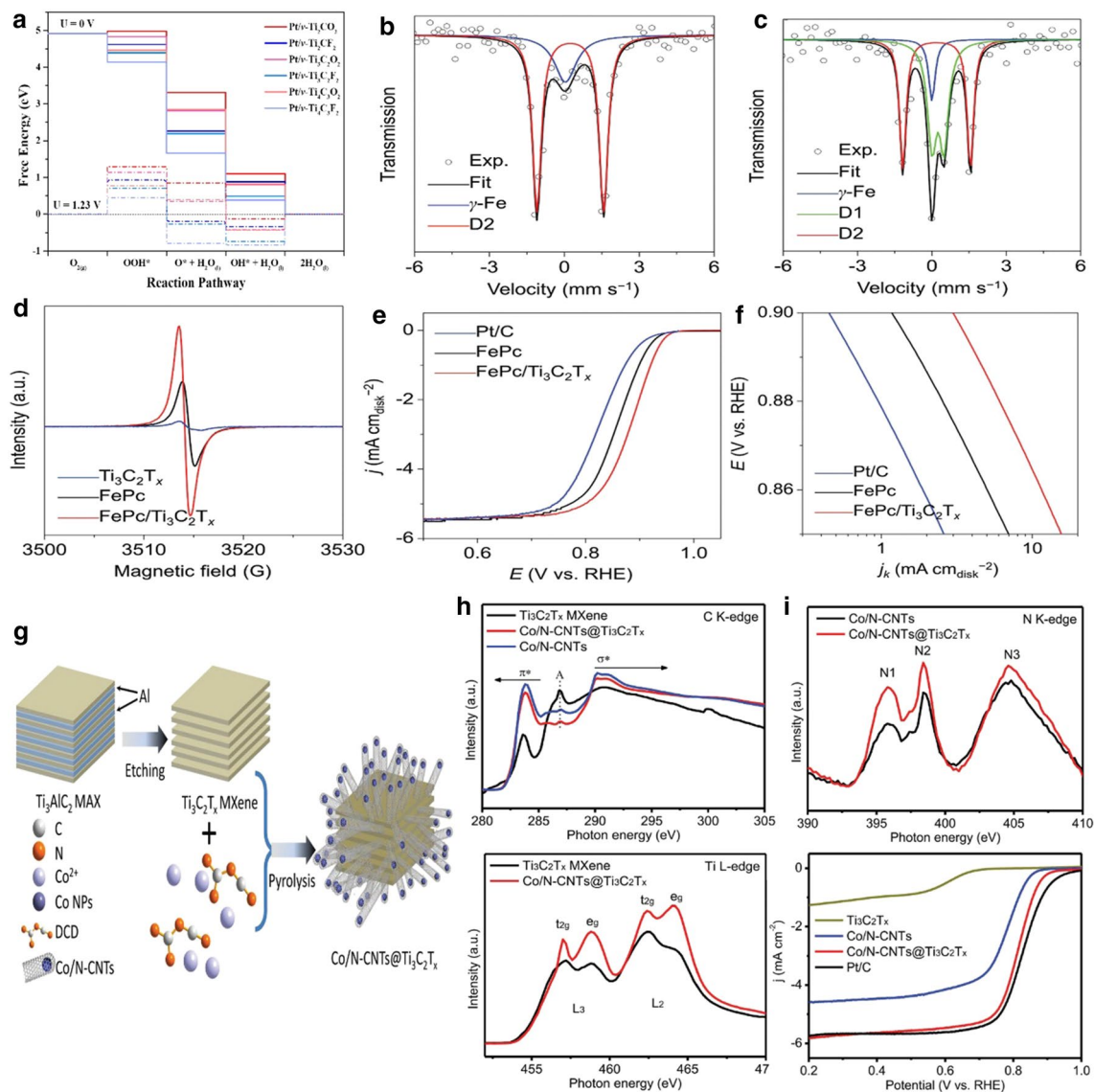
Fig. 10 **a** Free energy diagram of ORR intermediates on Pt/*v*-Ti$_{n+1}$C$_n$T$_2$ (*n* = 1–3, T = O or F) surfaces. Reproduced with permission [132]. Copyright 2019, American Chemical Society. **b** Fe Mössbauer transmission spectra and **c** deconvolution of pristine FePc and FePc/Ti$_3$C$_2$T$_x$. **d** X-band ESR spectra of pristine Ti$_3$C$_2$T$_x$, FePc, and FePc/Ti$_3$C$_2$T$_x$. **e** Polarization curves and **f** the corresponding Tafel plots of pristine FePc, FePc/Ti$_3$C$_2$T$_x$, and Pt/C. Reproduced with permission [48]. Copyright 2018, Wiley-VCH. **g** Preparation of Co/N-

CNTs@Ti$_3$C$_2$T$_x$ composites. **h** C K-edge XANES spectra of Ti$_3$C$_2$T$_x$ MXene, Co/N-CNTs@Ti$_3$C$_2$T$_x$, and Co/N-CNTs. **i** N K-edge XANES spectra of Co/N-CNTs and Co/N-CNTs@Ti$_3$C$_2$T$_x$. **j** Ti L-edge XANES spectra of Ti$_3$C$_2$T$_x$ MXene and Co/N-CNTs@Ti$_3$C$_2$T$_x$. **k** Polarization curves of Ti$_3$C$_2$T$_x$, Co/N-CNTs, Co/N-CNTs@Ti$_3$C$_2$T$_x$, and Pt/C. Reproduced with permission [111]. Copyright 2018, Wiley-VCH

Fig. 10e, f, the optimized hybrids showed lower half-wave potentials (− 0.886 vs. RHE) compared with pure FePc (− 0.886 vs. RHE) and commercial Pt/C (− 0.84 V vs. RHE). The catalysts also, respectively, showed two- and fivefold higher specific ORR activity than pure FePc and commercial Pt/C in 0.1 mol/L KOH solution.

Zhang et al. [111] presented a new type of Co/N-CNTs@$Ti_3C_2T_x$ hybrid synthesized by an in situ growth strategy (Fig. 10g). The resulting catalyst showed superior ORR catalytic performance with a low onset potential of 0.936 V versus RHE and a half-wave potential of 0.815 V versus RHE in 0.1 mol/L KOH aqueous solution (Fig. 10k); such performance was attributed to strong interfacial coupling and electron transfers in the composite, which were well verified by XANES (Fig. 10h–j). A series of nanohybrids, such as $Mn_3O_4/Ti_3C_2T_x$ nanocomposites [114], C_3N_4/Ti_3C_2 heterostructures [47], FeNC/MXene nanohybrids [112], urchin-like MXene-$Ag_{0.9}Ti_{0.1}$ nanowire composites [113], and FeCo (3:1)-N-d-Ti_3C_2 MXene hybrids [115], have also been proven to display outstanding ORR performance.

Nitrogen Reduction Reaction

NH_3 is considered a promising alternative energy carrier on account of its high energy density. At present, large-scale NH_3 production is primarily conducted via the Haber–Bosch method at high-pressure and high-temperature conditions using H_2 and nitrogen N_2 as the virgin gas. However, this process consumes large amounts of energy and generates massive amounts of CO_2. Thus, developing sustainable and economical N_2-fixation methods is urgently needed. Electrocatalytic NRR has attracted much attention due to its innate advantages, including reaction under ambient conditions and water as the hydrogen source [133]. However, NRR processes remain at the infant stages of development, and designs of efficient and low-cost electrocatalysts continue to challenge researchers.

MXene-based materials have recently been studied as catalysts for NRR. For example, Azofra et al. [50] predicted the N_2-capture behaviors of M_3C_2 MXenes using DFT calculations and found that V_3C_2 and Nb_3C_2 are excellent candidates as NRR catalysts due to their low reaction energies of 0.32 and 0.39 eV (vs. a standard hydrogen electrode), respectively (Fig. 11a). V_3C_2 showed a low activation barrier of 0.64 eV, which is smaller than that of Nb_3C_2 (0.85 eV), for the first proton–electron transfer (rate-determining step). Gao et al. [134] predicted the catalytic activity of a series of single atoms (i.e., Sc, Ti, V, Cr, Mn, Fe, Co, Ni, Cu, Zn, Mo, Ru, Rh, Pd, Ag, Cd, and Au) anchored onto $Ti_3C_2O_2$ by calculating their Gibbs free energies. The authors suggested that end-on N_2 adsorption is energetically advantageous and that negative free energies represent outstanding N_2 activation properties. Hydrogenations of N_2 into *NNH

and of *NH_2 into NH_3 were considered possible potential-limiting steps. In another study, Cheng et al. [135] carried out DFT calculations to investigate the catalytic activity of single transition metal atom (Mo, Mn, Fe, Co, Ni, or Cu)-decorated M_2NO_2-type MXenes (M = Ti, V, and Cr) for NRR. Mo/Ti_2NO_2 was screened as a very promising candidate catalyst with a low overpotential of 0.16 eV. This result could be ascribed to the strong bonding strength between Mo and Ti_2NO_2. Moreover, Mo/Ti_2NO_2 showed a low Gibbs free energy (0.12 eV) for NH_3 desorption, which promotes NH_3 release, and exhibited excellent metallic characteristics, which could effectively promote electron transfer between Mo and Ti_2NO_2. Zheng and co-workers [136] studied the NRR performance of single-atom B-decorated MXenes using DFT calculations. Here, B-doped Mo_2CO_2 and W_2CO_2 MXenes showed excellent catalytic activity and selectivity with limiting potentials of − 0.20 and − 0.24 V, respectively (Fig. 11b–d). Hydrogenation of *N_2 into *N_2H could be facilitated by the high tendency of B-to-adsorbate electron donation. However, conversion of *NH_2 into *NH_3 was seriously hindered by strong B–N bonding.

Some experiments have been performed to investigate the NRR activity of MXene-based materials. For example, Luo et al. [49] first verified that the central Ti atom in the MXene $Ti_3C_2T_x$ is the most active site for N_2 adsorption (1.34 eV) by comparison with C (− 0.16 eV), O (− 1.21 eV), and lateral Ti (− 0.95 eV) atoms. In addition, the basal plane of MXene is inert relative to edge planes owing to the former's lower exposure of Ti sites, as shown in Fig. 12a, b. When smaller $Ti_3C_2T_x$ MXenes were dispersed on vertically aligned metal FeOOH nanosheets, a faradaic efficiency of 5.78% under − 0.2 V versus RHE was obtained; this value is 1.25 times higher than the maximum value obtained from an MXene/stainless steel mesh (4.62%) under − 0.1 V versus RHE, as presented in Fig. 12c, d. Li and co-workers [118] directly applied small-sized (~ 50–100 nm) F-free $Ti_3C_2T_x$ nanosheets for NRR. The obtained catalyst showed an NH_3 yield of 36.9 μg/(h mg_{cat}) and faradaic efficiency of 9.1% at − 0.3 V versus RHE in 0.1 mol/L HCl (Fig. 12e). These values are, once again, much larger than those of F-based MXenes due to the unique size effect and fluorine-free characteristics to the novel catalysts. In another study, Zhao et al. [119] reported that $Ti_3C_2T_x$ MXene nanosheets could serve as catalysts for NRR. The catalysts achieved an NH_3 yield of 20.4 μg/(h mg_{cat}) and a faradaic efficiency of 9.3% at − 0.4 V versus RHE. DFT results demonstrated that the distal NRR mechanism was more favorable, and the related *NH_2/NH_3 reaction was the rate-determining step. Zhang et al. [117] prepared $TiO_2/Ti_3C_2T_x$ hybrids by using a simple hydrothermal method and studied their catalytic activity for NRR. The obtained hybrids were tested in 0.1 mol/L HCl and showed good catalytic performance with an NH_3 yield of 26.32 μg/(h mg_{cat}) and faradaic efficiency of 8.42% at − 0.60 V versus
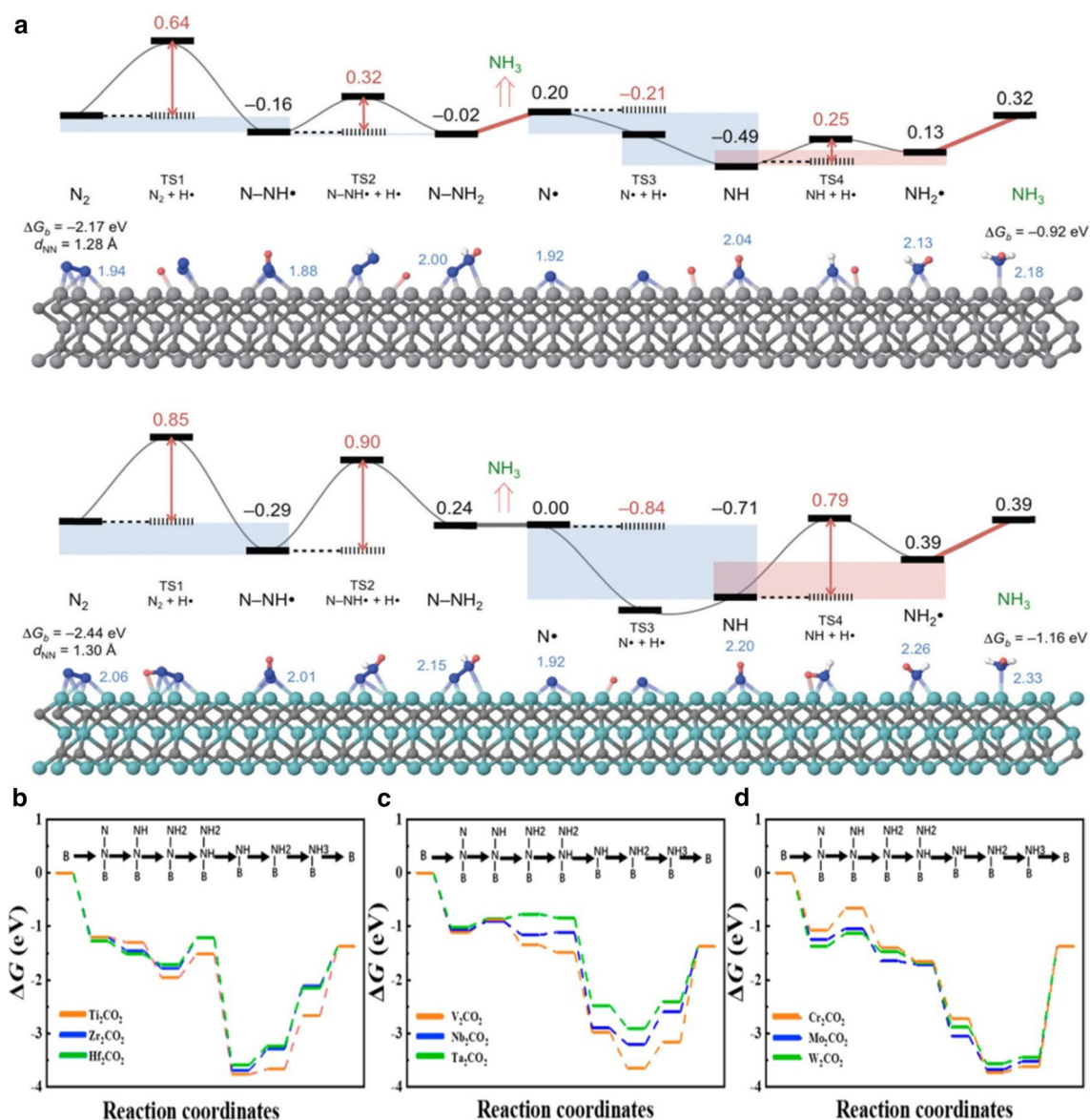
Fig. 11 **a** Minimum energy path for N_2 conversion into NH_3 catalyzed by V_3C_2 (top) and Nb_3C_2 (bottom) MXenes. Reproduced with permission [50]. Copyright 2016, Royal Society of Chemistry. Free energy profiles for the NRR catalyzed by group **b** IV (Ti, Zr, Hf), **c** V (V, Nb, Ta), and **d** VI (Cr, Mo, W) MXenes with B centers. Reproduced with permission [136]. Copyright 2019, American Chemical Society

RHE (Fig. 12f, g); these results are believed to originate from the synergistic effect between TiO_2 nanoparticles and $Ti_3C_2T_x$ nanosheets. Kong and co-workers [120] reported that an MnO_2-decorated $Ti_3C_2T_x$ MXene nanohybrid could serve as an electrocatalyst for NRR with excellent durability and outstanding selectivity. This nanohybrid showed a large NH_3 yield of 34.12 μg/(h mg$_{cat}$) and high faradaic efficiency of 11.39% under 0.55 V versus RHE in 0.1 mol/L HCl (Fig. 12h). As shown in Fig. 12i, DFT calculations indicated that unsaturated surface Mn atoms could serve as active sites for adsorption and activation of N_2. The first

hydrogenation process in this strategy was identified as the rate-determining step.

CO$_2$ Reduction Reaction

Large-scale anthropogenic CO_2 emissions cause serious environmental issues, including global warming and extinction of species, among others. Converting CO_2 by CO_2RR into value-added chemicals and fuels has attracted extensive research attention due to the environment-friendly characteristics of this technology [137, 138].
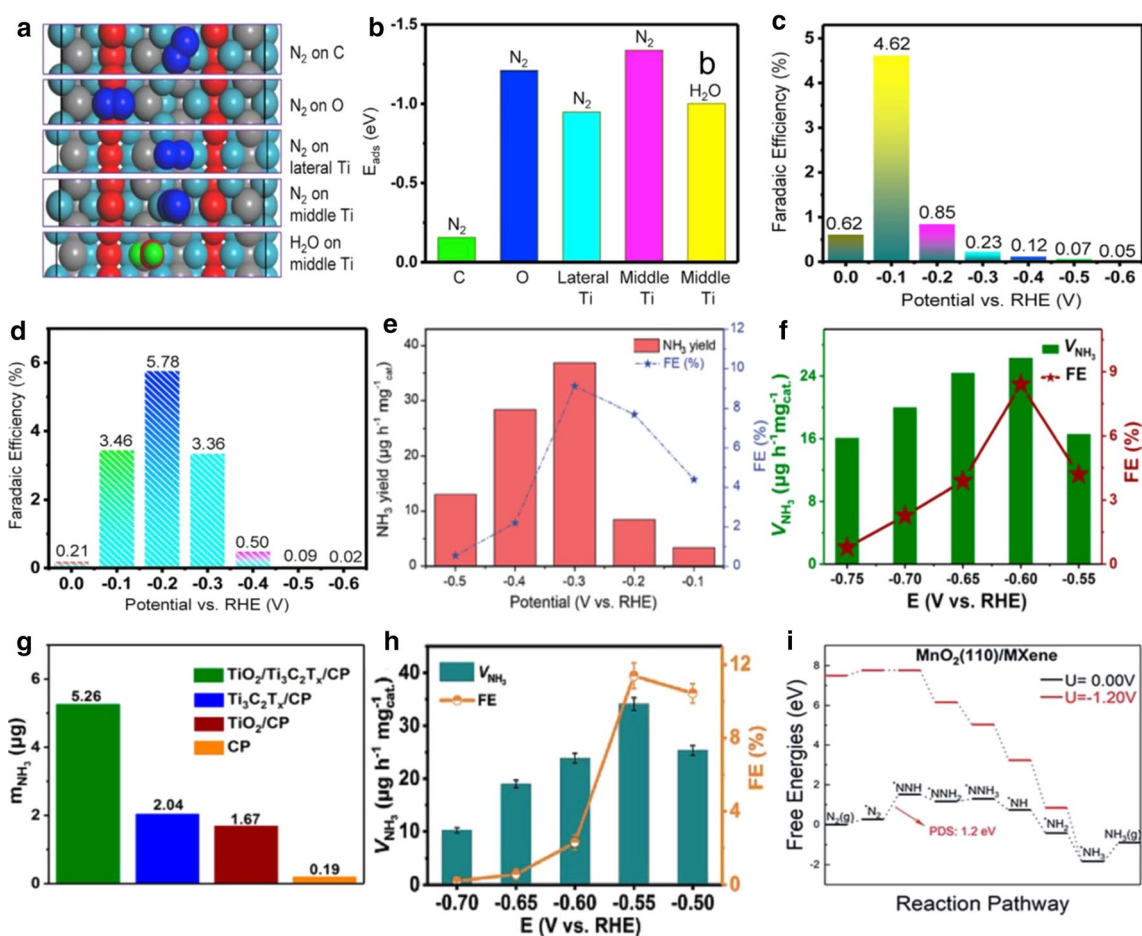
Fig. 12 a Optimized structures of $Ti_3C_2T_x$ MXenes and the corresponding adsorption energies for N_2 on various atomic sites and H_2O on the middle Ti atomic site. **b–d** Faradic efficiencies of a $Ti_3C_2T_x$ MXene/stainless steel mesh and $Ti_3C_2T_x$ MXene/FeOOH at different potentials, respectively. Reproduced with permission [49]. Copyright 2018, Elsevier Ltd. **e** NH_3 yields and faradaic efficiencies of F-free $Ti_3C_2T_x$ nanosheets and $Ti_3C_2T_x$/carbon paper at various potentials. Reproduced with permission [118]. Copyright 2019, Royal Society of Chemistry. **f** NH_3 yields and faradaic efficiencies of $TiO_2/Ti_3C_2T_x$ at various potentials. **g** Amounts of NH_3 obtained from carbon paper (CP), TiO_2/CP, $Ti_3C_2T_x$/CP, and $TiO_2/Ti_3C_2T_x$/CP at -0.6 V after 2 h of electrolysis. Reproduced with permission [117]. Copyright 2019, American Chemical Society. **h** NH_3 yields and faradaic efficiencies of $MnO_2–Ti_3C_2T_x$ at various potentials. **i** Gibbs free energy profiles for NRR over MnO_2 (110)–MXene surfaces through the traditional distal pathway. Reproduced with permission [120]. Copyright 2019, Royal Society of Chemistry

The electrocatalytic CO_2RR activity of MXenes has been explored by using theoretical DFT calculations. For example, Chen et al. [139] studied different −OH terminated MXenes for CO_2RR by theoretical calculation and found that $Sc_2C(OH)_2$ is a highly promising candidate for catalyzing the CO_2RR of CO_2 into CH_4 with a limiting potential of -0.53 V. This excellent performance could be attributed to the high reactivity of H atoms in the −OH termination groups of the MXene, which is conducive to the formation of stable structures with intermediates and lowering of the necessary overpotential. MXene catalysts with low charge migration during the potential-limiting step have also been suggested to demonstrate good CO_2RR performance. Li et al. [140] predicted that IV–VI series MXenes show excellent performance for CO_2 capture. Cr_3C_2 and Mo_3C_2

MXenes have been considered highly promising candidates for the selective conversion of CO_2 into CH_4. The authors also found that the formation process of OCHO· and HOCO· radicals occurs as a spontaneous reaction in the early hydrogenation steps, which was the rate-determining step of CO_2 into CH_4 conversion process. According to the calculated minimum energy path results, the $CO_2 \rightarrow CH_4$ conversion process over bare Cr_3C_2 and Mo_3C_2 required overpotentials of 1.05 and 1.31 eV, respectively (Fig. 13a, b). However, functional group (e.g., −O or −OH)-terminated MXenes (Mo_3C_2) required very low energy inputs (Fig. 13c, d). In another study, Handoko and co-workers [51] reported that W_2CO_2 and Ti_2CO_2 are highly promising M_2XO_2 MXene candidates for CO_2RR owing to their low overpotential and good selectivity. This excellent performance could be

Fig. 13 **a** Side view of the minimum energy path for CO_2 conversion into $*CH_4$ and $**H_2O$ catalyzed by Mo_3C_2. **b** Minimum energy path for CO_2 conversion into $*CH_4$ and $**H_2O$ catalyzed by Cr_3C_2. Minimum energy path for CO_2 conversion into CH_4 and H_2O over **c** $Mo_3C_2(OH)_2$ and **d** $Mo_3C_2O_2$. Reproduced with permission [140]. Copyright 2019, American Chemical Society
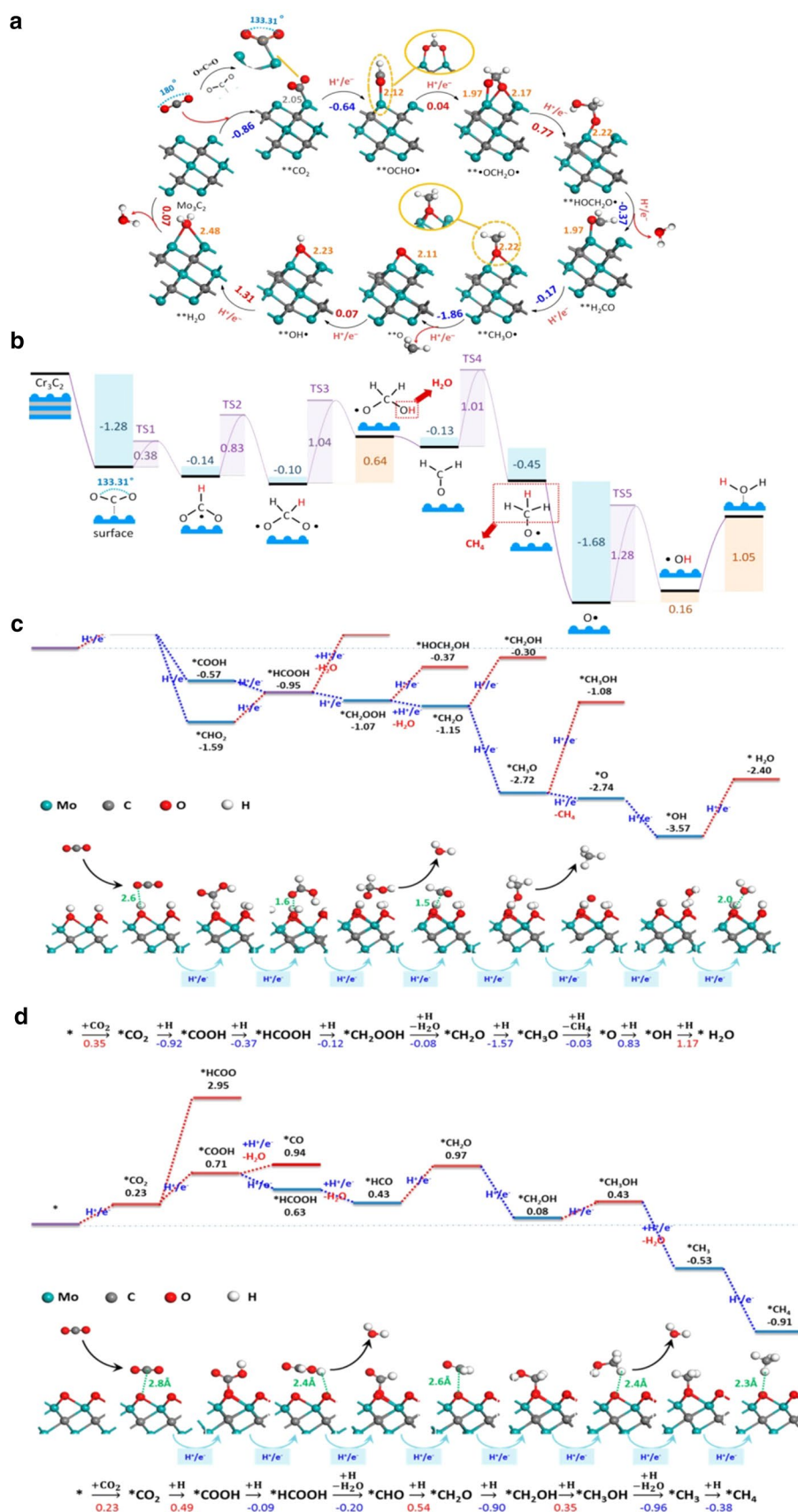
attributed to the accessibility of the *HCOOH pathway, which is energetically more favorable compared with *CO pathway. In addition, O termination groups on MXenes help stabilize the reaction intermediates. Thus far, however, no experimental study on MXene-based catalysts for CO_2RR has yet been reported.

Summary and Outlook

As an emerging class of 2D materials, MXenes show tremendous potential in electrochemical energy conversion. In this review, we systematically summarized recent advances in MXenes-based materials in electrocatalysis, including HER, OER, ORR, NRR, and CO_2RR. Many high-performance MXenes-based catalysts featuring distinct inherent properties, such as excellent metallic conductivity, rich surface chemistry, and unique morphology, have been prepared. We outlined two common strategies for improving the electrocatalytic property of MXene-based catalysts. First, surface functional groups (e.g., −O, −OH, and −F) and exposed terminal metal sites (e.g., Ti, Mo, Nb, and V) can serve as catalytic activity sites, as verified by theoretical calculations and experiments. Thus, regulating the surface chemistry of these molecules is a promising strategy to enhance the electrocatalytic property of MXenes. Second, constructing nanohybrids with other active components (e.g., nanoparticles, monoatomics, and other 2D materials) is another effective strategy to improve the electrocatalytic performance of MXene-based materials. The surface functional groups of MXenes endow them with the ability to easily form strong interactions with different components. Many metallic MXenes show enhanced charge-carrier transfer properties, and their 2D structure can prevent the active materials from aggregating.

Despite the initial successes obtained from MXene-based electrocatalysts, however, many challenges remain to be solved. For example, more novel MXenes must have been predicted and synthesized by theoretical calculations and experimental methods. The electrocatalytic performance of these materials should also be systematically investigated. The electrocatalytic performance of MXenes-based materials for some applications (e.g., CO_2RR) remains mostly theoretical. Thus, experimental studies should be performed to verify the results of theoretical calculations. Moreover, great efforts have been exerted to develop MXene-based catalysts for electrocatalysis, but elucidating the relevant catalytic mechanism has proven to be difficult. Therefore, more advanced characterizations (e.g., in situ microscopy and spectroscopy) and theoretical calculations must be conducted to promote the rational design of MXene-based catalysts.

References

1. Novoselov KS, Geim AK, Morozov SV et al (2004) Electric field effect in atomically thin carbon films. Science 306(5696):666–669
2. Bonaccorso F, Colombo L, Yu G et al (2015) 2D materials: graphene, related two-dimensional crystals, and hybrid systems for energy conversion and storage. Science 347(6217):1246501
3. Geng DC, Yang HY (2018) Recent advances in growth of novel 2D materials: beyond graphene and transition metal dichalcogenides. Adv Mater 30(45):e1800865
4. Feng RJ, Lei WY, Liu G et al (2018) Visible- and NIR-light responsive black-phosphorus-based nanostructures in solar fuel production and environmental remediation. Adv Mater 30(49):e1804770
5. Mendoza-Sánchez B, Gogotsi Y (2016) Synthesis of two-dimensional materials for capacitive energy storage. Adv Mater 28(29):6104–6135
6. Wang D, Wang ZG, Wang L et al (2015) Ultrathin membranes of single-layered MoS_2 nanosheets for high-permeance hydrogen separation. Nanoscale 7(42):17649–17652
7. Abraham J, Vasu KS, Williams CD et al (2017) Tunable sieving of ions using graphene oxide membranes. Nat Nanotechnol 12(6):546–550
8. Reina G, González-Domínguez JM, Criado A et al (2017) Promises, facts and challenges for graphene in biomedical applications. Chem Soc Rev 46(15):4400–4416
9. Fan XB, Xu PT, Zhou DK et al (2015) Fast and efficient preparation of exfoliated 2H MoS_2 nanosheets by sonication-assisted lithium intercalation and infrared laser-induced 1T to 2H phase reversion. Nano Lett 15(9):5956–5960
10. Fan XB, Xu PT, Li YC et al (2016) Controlled exfoliation of MoS_2 crystals into trilayer nanosheets. J Am Chem Soc 138(15):5143–5149
11. Hai X, Chang K, Pang H et al (2016) Engineering the edges of MoS_2 (WS_2) crystals for direct exfoliation into monolayers in polar micromolecular solvents. J Am Chem Soc 138(45):14962–14969
12. Liu H, Du YC, Deng YX et al (2015) Semiconducting black phosphorus: synthesis, transport properties and electronic applications. Chem Soc Rev 44(9):2732–2743
13. Ambrosi A, Sofer Z, Pumera M (2017) Electrochemical exfoliation of layered black phosphorus into phosphorene. Angew Chem 56(35):10443–10445
14. Yasaei P, Kumar B, Foroozan T et al (2015) High-quality black phosphorus atomic layers by liquid-phase exfoliation. Adv Mater 27(11):1887–1892
15. Li Z, Zhuang JC, Chen L et al (2016) Observation of van hove singularities in twisted silicene multilayers. ACS Cent Sci 2(8):517–521

16. Lang JL, Ding B, Zhang S et al (2017) Scalable synthesis of 2D Si nanosheets. Adv Mater 29(31):1701777

17. Ares P, Palacios JJ, Abellán G et al (2018) Recent progress on antimonene: a new bidimensional material. Adv Mater 30(2):1703771

18. Gibaja C, Rodriguez-San-Miguel D, Ares P et al (2016) Few-layer antimonene by liquid-phase exfoliation. Angew Chem 55(46):14345–14349

19. Zhu WS, Gao X, Li Q et al (2016) Controlled gas exfoliation of boron nitride into few-layered nanosheets. Angew Chem 55(36):10766–10770

20. Weng QH, Wang XB, Wang X et al (2016) Functionalized hexagonal boron nitride nanomaterials: emerging properties and applications. Chem Soc Rev 45(14):3989–4012

21. Luo W, Wang YB, Hitz E et al (2017) Solution processed boron nitride nanosheets: synthesis, assemblies and emerging applications. Adv Funct Mater 27(31):1701450

22. Yu JF, Wang Q, O'Hare D et al (2017) Preparation of two dimensional layered double hydroxide nanosheets and their applications. Chem Soc Rev 46(19):5950–5974

23. Anasori B, Lukatskaya MR, Gogotsi Y (2017) 2D metal carbides and nitrides (MXenes) for energy storage. Nat Rev Mater 2(2):16098

24. Sang XH, Xie Y, Lin MW et al (2016) Atomic defects in monolayer titanium carbide ($Ti_3C_2T_x$) MXene. ACS Nano 10(10):9193–9200

25. Li Z, Wu Y (2019) 2D early transition metal carbides (MXenes) for catalysis. Small 15(29):e1804736

26. Mashtalir O, Lukatskaya MR, Zhao MQ et al (2015) Amine-assisted delamination of Nb_2C MXene for Li-ion energy storage devices. Adv Mater 27(23):3501–3506

27. Lian P, Dong Y, Wu Z-S et al (2017) Alkalized Ti_3C_2 MXene nanoribbons with expanded interlayer spacing for high-capacity sodium and potassium ion batteries. Nano Energy 40:1–8

28. Tang Q, Zhou Z, Shen PW (2012) Are MXenes promising anode materials for Li ion batteries? Computational studies on electronic properties and Li storage capability of Ti_3C_2 and $Ti_3C_2X_2$ (X = F, OH) monolayer. J Am Chem Soc 134(40):16909–16916

29. Ashton M, Hennig RG, Sinnott SB (2016) Computational characterization of lightweight multilayer MXene Li-ion battery anodes. Appl Phys Lett 108(2):023901

30. Liu G, Zou J, Tang Q et al (2017) Surface modified Ti_3C_2 MXene nanosheets for tumor targeting photothermal/photodynamic/chemo synergistic therapy. ACS Appl Mater Interfaces 9(46):40077–40086

31. Lin H, Wang XG, Yu LD et al (2017) Two-dimensional ultrathin MXene ceramic nanosheets for photothermal conversion. Nano Lett 17(1):384–391

32. Dai C, Lin H, Xu G et al (2017) Biocompatible 2D titanium carbide (MXenes) composite nanosheets for pH-responsive MRI-guided tumor hyperthermia. Chem Mater 29(20):8637–8652

33. Peng C, Yang XF, Li YH et al (2016) Hybrids of two-dimensional Ti_3C_2 and TiO_2 exposing 001 facets toward enhanced photocatalytic activity. ACS Appl Mater Interfaces 8(9):6051–6060

34. Gao YP, Wang LB, Zhou AG et al (2015) Hydrothermal synthesis of TiO_2/Ti_3C_2 nanocomposites with enhanced photocatalytic activity. Mater Lett 150:62–64

35. Ran JR, Gao GP, Li FT et al (2017) Ti_3C_2 MXene co-catalyst on metal sulfide photo-absorbers for enhanced visible-light photocatalytic hydrogen production. Nat Commun 8:13907

36. Lin ZF, Barbara D, Taberna P-L et al (2016) Capacitance of $Ti_3C_2T_x$ MXene in ionic liquid electrolyte. J Power Sources 326:575–579

37. Dall'Agnese Y, Rozier P, Taberna P-L et al (2016) Capacitance of two-dimensional titanium carbide (MXene) and MXene/carbon nanotube composites in organic electrolytes. J Power Sources 306:510–515

38. Ghidiu M, Lukatskaya MR, Zhao MQ et al (2014) Conductive two-dimensional titanium carbide 'clay' with high volumetric capacitance. Nature 516(7529):78–81

39. Ding L, Wei YY, Li LB et al (2018) MXene molecular sieving membranes for highly efficient gas separation. Nat Commun 9(1):155

40. Berdiyorov GR, Madjet ME, Mahmoud KA (2016) Ionic sieving through $Ti_3C_2(OH)_2$ MXene: first-principles calculations. Appl Phys Lett 108(11):113110

41. Ding L, Wei YY, Wang YJ et al (2017) A two-dimensional lamellar membrane: MXene nanosheet stacks. Angew Chem 56(7):1825–1829

42. Liu JP, Liu YZ, Xu DY et al (2019) Hierarchical "nanoroll" like $MoS_2/Ti_3C_2T_x$ hybrid with high electrocatalytic hydrogen evolution activity. Appl Catal B Environ 241:89–94

43. Du CF, Sun XL, Yu H et al (2019) Synergy of Nb doping and surface alloy enhanced on water-alkali electrocatalytic hydrogen generation performance in Ti-based MXene. Adv Sci 6(11):1900116

44. Jiang YN, Sun T, Xie X et al (2019) Oxygen-functionalized ultrathin $Ti_3C_2T_x$ MXene for enhanced electrocatalytic hydrogen evolution. Chemsuschem 12(7):1368–1373

45. Yu MZ, Zhou S, Wang ZY et al (2018) Boosting electrocatalytic oxygen evolution by synergistically coupling layered double hydroxide with MXene. Nano Energy 44:181–190

46. Liu JP, Chen T, Juan P et al (2018) Hierarchical cobalt borate/MXenes hybrid with extraordinary electrocatalytic performance in oxygen evolution reaction. Chemsuschem 11(21):3758–3765

47. Yu XL, Yin WC, Wang T et al (2019) Decorating g-C_3N_4 nanosheets with Ti_3C_2 MXene nanoparticles for efficient oxygen reduction reaction. Langmuir 35(8):2909–2916

48. Li ZL, Zhuang ZC, Lv F et al (2018) The marriage of the FeN_4 moiety and MXene boosts oxygen reduction catalysis: Fe 3d electron delocalization matters. Adv Mater 30(43):e1803220

49. Luo Y, Chen G-F, Ding L et al (2019) Efficient electrocatalytic N_2 fixation with MXene under ambient conditions. Joule 3(1):279–289

50. Azofra LM, Li N, MacFarlane DR et al (2016) Promising prospects for 2D d^2–d^4 M_3C_2 transition metal carbides (MXenes) in N_2 capture and conversion into ammonia. Energy Environ Sci 9(8):2545–2549

51. Handoko AD, Khoo KH, Tan TL et al (2018) Establishing new scaling relations on two-dimensional MXenes for CO_2 electroreduction. J Mater Chem A 6(44):21885–21890

52. Zhao D, Chen Z, Yang WJ et al (2019) MXene (Ti_3C_2) vacancy-confined single-atom catalyst for efficient functionalization of CO_2. J Am Chem Soc 141(9):4086–4093

53. Pang JB, Mendes RG, Bachmatiuk A et al (2019) Applications of 2D MXenes in energy conversion and storage systems. Chem Soc Rev 48(1):72–133

54. Li XQ, Wang CY, Cao Y et al (2018) Functional MXene materials: progress of their applications. Chem Asian J 13(19):2742–2757

55. Zhang X, Zhang ZH, Zhou Z (2018) MXene-based materials for electrochemical energy storage. J Energy Chem 27(1):73–85

56. Handoko AD, Steinmann SN, Seh ZW (2019) Theory-guided materials design: two-dimensional MXenes in electro- and photocatalysis. Nanoscale Horiz 4(4):809–827

57. Naguib M, Kurtoglu M, Presser V et al (2011) Two-dimensional nanocrystals produced by exfoliation of Ti_3AlC_2. Adv Mater 23(37):4248–4253

58. Liang X, Garsuch A, Nazar LF (2015) Sulfur cathodes based on conductive MXene nanosheets for high-performance lithium-sulfur batteries. Angew Chem 54(13):3907–3911

59. Du F, Tang H, Pan LM et al (2017) Environmental friendly scalable production of colloidal 2D titanium carbonitride MXene with minimized nanosheets restacking for excellent cycle life lithium-ion batteries. Electrochim Acta 235:690–699

60. Naguib M, Mashtalir O, Carle J et al (2012) Two-dimensional transition metal carbides. ACS Nano 6(2):1322–1331

61. Halim J, Kota S, Lukatskaya MR et al (2016) Synthesis and characterization of 2D molybdenum carbide (MXene). Adv Funct Mater 26(18):3118–3127

62. Anasori B, Dahlqvist M, Halim J et al (2015) Experimental and theoretical characterization of ordered MAX phases Mo_2TiAlC_2 and $Mo_2Ti_2AlC_3$. J Appl Phys 118(9):094304

63. Zhou J, Zha XH, Chen FY et al (2016) A two-dimensional zirconium carbide by selective etching of Al_3C_3 from nanolaminated $Zr_3Al_3C_5$. Angew Chem 128(16):5092–5097

64. Zhou J, Zha XH, Zhou XB et al (2017) Synthesis and electrochemical properties of two-dimensional hafnium carbide. ACS Nano 11(4):3841–3850

65. Yang J, Naguib M, Ghidiu M et al (2016) Two-dimensional Nb-based M_4C_3 solid solutions (MXenes). J Am Ceram Soc 99(2):660–666

66. Wu M, Wang BX, Hu QK et al (2018) The synthesis process and thermal stability of V_2C MXene. Materials 11(11):2112

67. Wang X, Garnero C, Rochard G et al (2017) A new etching environment (FeF_3/HCl) for the synthesis of two-dimensional titanium carbide MXenes: a route towards selective reactivity vs. water. J Mater Chem A 5(41):22012–22023

68. Wang LB, Zhang H, Wang B et al (2016) Synthesis and electrochemical performance of $Ti_3C_2T_x$ with hydrothermal process. Electron Mater Lett 12(5):702–710

69. Feng AH, Yu Y, Wang Y et al (2017) Two-dimensional MXene Ti_3C_2 produced by exfoliation of Ti_3AlC_2. Mater Des 114:161–166

70. Urbankowski P, Anasori B, Makaryan T et al (2016) Synthesis of two-dimensional titanium nitride Ti_4N_3 (MXene). Nanoscale 8(22):11385–11391

71. Lipatov A, Alhabeb M, Lukatskaya MR et al (2016) Effect of synthesis on quality, electronic properties and environmental stability of individual monolayer Ti_3C_2 MXene flakes. Adv Electron Mater 2(12):1600255

72. Xuan JN, Wang ZQ, Chen YY et al (2016) Organic-base-driven intercalation and delamination for the production of functionalized titanium carbide nanosheets with superior photothermal therapeutic performance. Angew Chem 55(47):14569–14574

73. Li GN, Tan L, Zhang YM et al (2017) Highly efficiently delaminated single-layered MXene nanosheets with large lateral size. Langmuir 33(36):9000–9006

74. Pang SY, Wong YT, Yuan SG et al (2019) Universal strategy for HF-free facile and rapid synthesis of two-dimensional MXenes as multifunctional energy materials. J Am Chem Soc 141(24):9610–9616

75. Li M, Lu J, Luo K et al (2019) Element replacement approach by reaction with Lewis acidic molten salts to synthesize nanolaminated MAX phases and MXenes. J Am Chem Soc 141(11):4730–4737

76. Chen XF, Zhu YZ, Zhang M et al (2019) N-butyllithium-treated $Ti_3C_2T_x$ MXene with excellent pseudocapacitor performance. ACS Nano 13(8):9449–9456

77. Hu T, Li ZJ, Hu MM et al (2017) Chemical origin of termination-functionalized MXenes: $Ti_3C_2T_2$ as a case study. J Phys Chem C 121(35):19254–19261

78. Fu ZH, Zhang QF, Legut D et al (2016) Stabilization and strengthening effects of functional groups in two-dimensional titanium carbide. Phys Rev B 94(10):104103

79. Meng QQ, Ma JL, Zhang YH et al (2018) The S-functionalized Ti_3C_2 Mxene as a high capacity electrode material for Na-ion batteries: a DFT study. Nanoscale 10(7):3385–3392

80. Wang XF, Shen X, Gao YR et al (2015) Atomic-scale recognition of surface structure and intercalation mechanism of Ti_3C_2X. J Am Chem Soc 137(7):2715–2721

81. Karlsson LH, Birch J, Halim J et al (2015) Atomically resolved structural and chemical investigation of single MXene sheets. Nano Lett 15(8):4955–4960

82. Hope MA, Forse AC, Griffith KJ et al (2016) NMR reveals the surface functionalisation of Ti_3C_2 MXene. Phys Chem Chem Phys 18(7):5099–5102

83. Harris KJ, Bugnet M, Naguib M et al (2015) Direct measurement of surface termination groups and their connectivity in the 2D MXene V_2CT_x using NMR spectroscopy. J Phys Chem C 119(24):13713–13720

84. Fredrickson KD, Anasori B, Seh ZW et al (2016) Effects of applied potential and water intercalation on the surface chemistry of Ti_2C and Mo_2C MXenes. J Phys Chem C 120(50):28432–28440

85. Wang G, Liao Y (2017) Theoretical prediction of robust and intrinsic half-metallicity in Ni_2N MXene with different types of surface terminations. Appl Surf Sci 426:804–811

86. Enyashin AN, Ivanovskii AL (2012) Atomic structure, comparative stability and electronic properties of hydroxylated Ti_2C and Ti_3C_2 nanotubes. Comput Theor Chem 989:27–32

87. Zhao SJ, Kang W, Xue JM (2015) MXene nanoribbons. J Mater Chem C 3(4):879–888

88. Halim J, Lukatskaya MR, Cook KM et al (2014) Transparent conductive two-dimensional titanium carbide epitaxial thin films. Chem Mater 26(7):2374–2381

89. Lai S, Jeon J, Jang SK et al (2015) Surface group modification and carrier transport properties of layered transition metal carbides (Ti_2CT_x, T: –OH, –F and –O). Nanoscale 7(46):19390–19396

90. Seh ZW, Fredrickson KD, Anasori B et al (2016) Two-dimensional molybdenum carbide (MXene) as an efficient electrocatalyst for hydrogen evolution. ACS Energy Lett 1(3):589–594

91. Handoko AD, Fredrickson KD, Anasori B et al (2018) Tuning the basal plane functionalization of two-dimensional metal carbides (MXenes) to control hydrogen evolution activity. ACS Appl Energy Mater 1(1):173–180

92. Li S, Tuo P, Xie JF et al (2018) Ultrathin MXene nanosheets with rich fluorine termination groups realizing efficient electrocatalytic hydrogen evolution. Nano Energy 47:512–518

93. Tran MH, Schäfer T, Shahraei A et al (2018) Adding a new member to the MXene family: synthesis, structure, and electrocatalytic activity for the hydrogen evolution reaction of $V_4C_3T_x$. ACS Appl Energy Mater 1(8):3908–3914

94. Yoon Y, Tiwari AP, Lee M et al (2018) Enhanced electrocatalytic activity by chemical nitridation of two-dimensional titanium carbide MXene for hydrogen evolution. J Mater Chem A 6(42):20869–20877

95. Yuan W, Cheng LF, An YR et al (2018) MXene nanofibers as highly active catalysts for hydrogen evolution reaction. ACS Sustain Chem Eng 6(7):8976–8982

96. Li Z, Qi ZY, Wang SW et al (2019) In situ formed Pt_3Ti nanoparticles on a two-dimensional transition metal carbide (MXene) used as efficient catalysts for hydrogen evolution reactions. Nano Lett 19(8):5102–5108

97. Yuan YY, Li HS, Wang LG et al (2019) Achieving highly efficient catalysts for hydrogen evolution reaction by electronic

state modification of platinum on versatile $Ti_3C_2T_x$ (MXene). ACS Sustain Chem Eng 7(4):4266–4273

98. Liang JM, Ding CY, Liu JP et al (2019) Heterostructure engineering of Co-doped MoS_2 coupled with Mo_2CT_x MXene for enhanced hydrogen evolution in alkaline media. Nanoscale 11(22):10992–11000

99. Filip J, Zavahir S, Lorencova L et al (2019) Tailoring electrocatalytic properties of Pt nanoparticles grown on $Ti_3C_2T_x$ MXene surface. J Electrochem Soc 166(2):H54–H62

100. Attanayake NH, Abeyweera SC, Thenuwara AC et al (2018) Vertically aligned MoS_2 on Ti_3C_2 (MXene) as an improved HER catalyst. J Mater Chem A 6(35):16882–16889

101. Cui BB, Hu B, Liu JM et al (2018) Solution-plasma-assisted bimetallic oxide alloy nanoparticles of Pt and Pd embedded within two-dimensional $Ti_3C_2T_x$ nanosheets as highly active electrocatalysts for overall water splitting. ACS Appl Mater Interfaces 10(28):23858–23873

102. Du C-F, Dinh KN, Liang QH et al (2018) Self-assemble and in situ formation of $Ni_{1-x}Fe_xPS_3$ nanomosaic-decorated MXene hybrids for overall water splitting. Adv Energy Mater 8(26):1801127

103. Wu XH, Wang ZY, Yu MZ et al (2017) Stabilizing the MXenes by carbon nanoplating for developing hierarchical nanohybrids with efficient lithium storage and hydrogen evolution capability. Adv Mater 29(24):1607017

104. Zhang JQ, Zhao YF, Guo X et al (2018) Single platinum atoms immobilized on an MXene as an efficient catalyst for the hydrogen evolution reaction. Nat Catal 1(12):985–992

105. Xiu LY, Wang ZY, Yu MZ et al (2018) Aggregation-resistant 3D MXene-based architecture as efficient bifunctional electrocatalyst for overall water splitting. ACS Nano 12(8):8017–8028

106. Wen YY, Wei ZT, Ma C et al (2019) MXene boosted CoNi-ZIF-67 as highly efficient electrocatalysts for oxygen evolution. Nanomaterials 9(5):775

107. Zhao L, Dong BL, Li SZ et al (2017) Interdiffusion reaction-assisted hybridization of two-dimensional metal-organic frameworks and $Ti_3C_2T_x$ nanosheets for electrocatalytic oxygen evolution. ACS Nano 11(6):5800–5807

108. Ma TY, Cao JL, Jaroniec M et al (2016) Interacting carbon nitride and titanium carbide nanosheets for high-performance oxygen evolution. Angew Chem 55(3):1138–1142

109. Tang Y, Yang CH, Yang YW et al (2019) Three dimensional hierarchical network structure of $S-NiFe_2O_4$ modified few-layer titanium carbides (MXene) flakes on nickel foam as a high efficient electrocatalyst for oxygen evolution. Electrochim Acta 296:762–770

110. Zou HY, He BW, Kuang PY et al (2018) Metal-organic framework-derived nickel–cobalt sulfide on ultrathin Mxene nanosheets for electrocatalytic oxygen evolution. ACS Appl Mater Interfaces 10(26):22311–22319

111. Zhang YK, Jiang HL, Lin YX et al (2018) In situ growth of cobalt nanoparticles encapsulated nitrogen-doped carbon nanotubes among $Ti_3C_2T_x$(MXene) matrix for oxygen reduction and evolution. Adv Mater Interfaces 5(16):1800392

112. Wen YY, Ma C, Wei ZT et al (2019) FeNC/MXene hybrid nanosheet as an efficient electrocatalyst for oxygen reduction reaction. RSC Adv 9(24):13424–13430

113. Zhang ZW, Li HN, Zou GD et al (2016) Self-reduction synthesis of new MXene/Ag composites with unexpected electrocatalytic activity. ACS Sustain Chem Eng 4(12):6763–6771

114. Xue Q, Pei ZX, Huang Y et al (2017) Mn_3O_4 nanoparticles on layer-structured Ti_3C_2 MXene towards the oxygen reduction reaction and zinc–air batteries. J Mater Chem A 5(39):20818–20823

115. Chen LG, Lin YX, Fu JY et al (2018) Hybridization of binary non-precious-metal nanoparticles with d-Ti_3C_2 MXene for catalyzing the oxygen reduction reaction. ChemElectroChem 5(21):3307–3314

116. Lin H, Chen LS, Lu XY et al (2019) Two-dimensional titanium carbide MXenes as efficient non-noble metal electrocatalysts for oxygen reduction reaction. Sci China Mater 62(5):662–670

117. Zhang J, Yang L, Wang HB et al (2019) In situ hydrothermal growth of TiO_2 nanoparticles on a conductive $Ti_3C_2T_x$ MXene nanosheet: a synergistically active Ti-based nanohybrid electrocatalyst for enhanced N_2 reduction to NH_3 at ambient conditions. Inorg Chem 58(9):5414–5418

118. Li TF, Yan XD, Huang LJ et al (2019) Fluorine-free $Ti_3C_2T_x$ (T = O, OH) nanosheets (~ 50–100 nm) for nitrogen fixation under ambient conditions. J Mater Chem A 7(24):14462–14465

119. Zhao JX, Zhang L, Xie X-Y et al (2018) $Ti_3C_2T_x$ (T = F, OH) MXene nanosheets: conductive 2D catalysts for ambient electrohydrogenation of N_2 to NH_3. J Mater Chem A 6(47):24031–24035

120. Kong WH, Gong FF, Zhou Q et al (2019) An MnO_2–$Ti_3C_2T_x$ MXene nanohybrid: an efficient and durable electrocatalyst toward artificial N_2 fixation to NH_3 under ambient conditions. J Mater Chem A 7(32):18823–18827

121. Zou XX, Zhang Y (2015) Noble metal-free hydrogen evolution catalysts for water splitting. Chem Soc Rev 44(15):5148–5180

122. Di J, Yan C, Handoko AD et al (2018) Ultrathin two-dimensional materials for photo- and electrocatalytic hydrogen evolution. Mater Today 21(7):749–770

123. Gao GP, O'Mullane AP, Du A (2017) A new family of promising catalysts for the hydrogen evolution reaction. ACS Catal 7(1):494–500

124. Cheng YW, Wang LJ, Li Y et al (2019) Etching and exfoliation properties of Cr_2AlC into Cr_2CO_2 and the electrocatalytic performances of 2D Cr_2CO_2 MXene. J Phys Chem C 123(25):15629–15636

125. Yang XW, Gao N, Zhou S et al (2018) MXene nanoribbons as electrocatalysts for the hydrogen evolution reaction with fast kinetics. Phys Chem Chem Phys 20(29):19390–19397

126. You JX, Si C, Zhou J et al (2019) Contacting MoS_2 to MXene: vanishing p-type Schottky barrier and enhanced hydrogen evolution catalysis. J Phys Chem C 123(6):3719–3726

127. Ling FL, Kang W, Jing HR et al (2019) Enhancing hydrogen evolution on the basal plane of transition metal dichacolgenide van der Waals heterostructures. NPJ Comput Mater 5(1):20

128. Zhou S, Yang XW, Pei W et al (2018) Heterostructures of MXenes and N-doped graphene as highly active bifunctional electrocatalysts. Nanoscale 10(23):10876–10883

129. Li PK, Zhu JG, Handoko AD et al (2018) High-throughput theoretical optimization of the hydrogen evolution reaction on MXenes by transition metal modification. J Mater Chem A 6(10):4271–4278

130. Shi QR, Zhu CZ, Du D et al (2019) Robust noble metal-based electrocatalysts for oxygen evolution reaction. Chem Soc Rev 48(12):3181–3192

131. Zheng Y, Jiao Y, Jaroniec M et al (2012) Nanostructured metal-free electrochemical catalysts for highly efficient oxygen reduction. Small 8(23):3550–3566

132. Liu CY, Li EY (2019) Termination effects of Pt/v-Ti$_{n+1}$C$_n$T$_2$ MXene surfaces for oxygen reduction reaction catalysis. ACS Appl Mater Interfaces 11(1):1638–1644
133. Tang C, Qiao SZ (2019) How to explore ambient electrocatalytic nitrogen reduction reliably and insightfully. Chem Soc Rev 48(12):3166–3180
134. Gao YJ, Zhuo H, Cao YY et al (2019) A theoretical study of electrocatalytic ammonia synthesis on single metal atom/MXene. Chin J Catal 40(2):152–159
135. Cheng YW, Dai JH, Song Y et al (2019) Single molybdenum atom anchored on 2D Ti$_2$NO$_2$ MXene as a promising electrocatalyst for N$_2$ fixation. Nanoscale 11(39):18132–18141
136. Zheng S, Li S, Mei Z et al (2019) Electrochemical nitrogen reduction reaction performance of single-boron catalysts tuned by MXene substrates. J Phys Chem Lett 10(22):6984–6989
137. Zhang L, Zhao ZJ, Gong JL (2017) Nanostructured materials for heterogeneous electrocatalytic CO$_2$ reduction and their related reaction mechanisms. Angew Chem 56(38):11326–11353
138. Handoko AD, Wei FX et al (2018) Understanding heterogeneous electrocatalytic carbon dioxide reduction through operando techniques. Nat Catal 1(12):922–934
139. Chen HT, Handoko AD, Xiao JW et al (2019) Catalytic effect on CO$_2$ electroreduction by hydroxyl-terminated two-dimensional MXenes. ACS Appl Mater Interfaces 11(40):36571–36579
140. Li N, Chen XZ, Ong WJ et al (2017) Understanding of electrochemical mechanisms for CO$_2$ capture and conversion into hydrocarbon fuels in transition-metal carbides (MXenes). ACS Nano 11(11):10825–10833

Xiaobin Fan is currently a professor at Tianjin University, China. His research interests include the preparation and applications of new nanomaterials and green chemistry.